# Theoretical and numerical stress analysis at edges of interacting faults: application to quasi-static fault propagation modelling

P. Favreau, S. Wolf

*Geophys. J. Int.* (2009) **179,** 733–750 doi: 10.1111/j.1365-246X.2009.04314.x

# Theoretical and numerical stress analysis at edges of interacting faults: application to quasi-static fault propagation modelling

P. Favreau[1] and S. Wolf[2]

[1] *Institut de Physique du Globe de Paris* – CNRS UMR 7154, 4 *Place Jussieu,* 75252 *Paris Cedex* 05, *France. E-mail: pfavre@ipgp.jussieu.fr*
[2] *Institut des Sciences de la Terre de Paris, Université Pierre et Marie Curie* – CNRS UMR 7193, 4 *Place Jussieu,* 75252 *Paris Cedex* 05, *France*

Accepted 2009 June 23. Received 2009 June 16; in original form 2007 August 28

## SUMMARY

We study theoretically and numerically the process of fault interactions within a quasi-static faulting model at long, tectonic timescale. The model handles birth, growth and sliding of multiple straight but non-coplanar interacting faults, regardless of any coseismic dynamic slip events. The study is restricted to the 2-D elastic antiplane case, an idealization of the normal faulting process. The model handles a general slip-dependent friction law for faults, to take into account a possible long-term fault weakening process. At fault tips, finite stress and progressive weakening lead to fault tip cohesive zones and ensure stability. We introduce a new numerical method based on a series development of slip profiles using a Chebyshev basis, which provides an accurate computation of large stress gradients at fault tips. Here simulations are limited to two parallel faults, which is enough to investigate many important features such as slip partitioning between faults, variable fault tip velocities and the state of stress in fault relay zones, responsible for the fault linking process. We study both a quasi-static problem and the associated spectral problem and show the link between them. We compare our quasi-static simulations with experimental results concerning the acceleration/deceleration of fault tips submitted to stress interaction and concerning the geometrical parameters that favour the linking of two normal faults. We find that the linking (coalescence) process should most likely occur during the deceleration phase of the faults tips subject to stress shadowing in the fault relay. Furthermore, for large ratios of fault lengths to separation, the linking process should begin for fault overlaps comparable to the values observed by Soliva & Benedicto in small natural fault relays (typically 2.9 times the fault separation).

**Key words:** Numerical solutions; Instability analysis; Dynamics and mechanics of faulting; Rheology and friction of fault zones.

## 1 INTRODUCTION

The faults are zones of highly localized deformation that builds up over a large, tectonic timescale. As localization increases, presumably through damaging and fracture coalescence, faults can be viewed as discontinuities in the crust, where large measurable slip takes place. The occurrence of earthquakes, at the timescale of seconds, is the sign that local and maybe larger slip instabilities can take place on faults, due to their effective weakening rheology. Another fundamental fact is that faults are organized in complex networks of segments of different importance. Fault birth, propagation, coalescence and activity have been studied with very different models and techniques. For example, if one focuses on the crust mechanics rather than the details of faulting, Ben-Zion *et al.* (1999) or Narteau (2007) have modelled fault propagation and coalescence by assimilating faults to the highly damaged zones of their models. These global models reveal statistical properties of fracture networks but they do not really model neither faults nor slip profiles. In a model that creates faulting more explicitly, Spyropoulos *et al.* (2002) used a discrete system of springs and separable blocks (the separation of the blocks giving the local slip) to model crust damage and fault formation: they show how fault interaction influences the development of faults and slip growth.

Although faults are heterogeneous objects resulting from complex mechanical and physical processes, they are not completely disordered objects and therefore they can be characterized by large-scale measurements of their geometry and cumulative slip. In that sense, it seems reasonable to study some aspects of faulting in the context of fracture growth as Lin & Parmentier (1988) or Baud & Reuschlé (1997) did for a single fault, or Kame *et al.* (2008) for a single fault in elastic layered media. However, concurrent fractures influence each other through the stress variations that they generate and this leads to numerous still open questions about the possible shapes of their slip profiles, the velocities of the fault tips, the state of stress at their tips, the state of stress in relay zones, and finally how much faults overlap before they link and coalesce to form larger faults (see Peacock 2002, for a review of these questions). Some of these questions have been investigated theoretically

by Segall & Pollard (1980) with a numerical model of 2-D strike slip (in-plane) interacting cracks subject to Coulomb friction, in an elastic body. The same numerical problem has been considered in full 3-D models by Willemse (1997) and Crider & Pollard (1998) to compute stress fields in en-echelon normal fault networks. These models produce a single snapshot of the mechanical equilibrium and do not model fault propagation itself. Past studies have shown that the modelling of the mechanical state of a fault requires to include several physical ingredients. A post-failure criterion is necessary to avoid the classical elastic square-root type singularity at fault tips and be consistent with finite material strength and finite stress in the faulting model. Cowie & Scholz (1992) used the Dugdale model (see Barrenblatt 1962) to fit accumulated fault slip observations. Post-failure criterion also induces a cohesive zone that produces smoother slip gradients at fault tips. Martel (1997) pointed out the importance of the cohesive zone on the stress distribution around fault tips and inside fault relays. Indeed, since a cohesive zone cancels the stress singularity, then, compared to the singular crack model, it can produce a very different stress field around fault tips. Peacock & Sanderson (1991) were the first to observe the effect of stress interaction on observed fault displacements and, using the Dugdale model, Gupta & Scholz (2000) quantified the intensity of the interaction of two non-coplanar parallel faults with respects to the geometry (fault length, separation and offset); but their model of fault growth remained conceptual.

With a 2-D elastic antiplane fault model with slip dependent friction, similar to the Palmer & Rice (1973) post-failure criterion, Wolf *et al.* (2006) modelled slip profiles (and the corresponding states of stress) through an unusual eigenmode analysis, first developed in Ionescu & Wolf 2005). In their model, fault tips are not supposed to move and therefore square-root singularities are *a priori* expected. However their parametric study on the geometry of two identical parallel non-coplanar faults shows that, when the overlap exceeds some critical value, the slip partitioning between both faults naturally looses its symmetry (one of the faults dominates the other). This bifurcation occurs when the frictional condition on faults is an active constraint of the problem, which therefore becomes non-linear (see Ionescu & Wolf 2005; Wolf *et al.* 2006, for more technical details). More precisely, in their eigenmode analysis, as one fault overlaps the other, it can create a stress shadow such that the neighbouring tip of the other fault is forced to remain stuck to respect the frictional threshold. Although their model is not built to cancel stress singularities at fault edges, the existence of a stuck zone on one of the faults clearly indicates that a non-singular stress field naturally takes place at the shadowed tip of the dominated fault. They extrapolated their results and conjectured that, in true quasi-static models and maybe in field observations, the stress shadowing could simply stop the progression of the shadowed fault tip. In addition, stress interaction was proved to have a strong influence on the existence of linear slip profiles inside shadow zones. Also, only using the geometry of some natural fault network in Afar, they were able to reproduce the large scale properties of the observed slip profiles, provided that they use variable fault weakening coefficients along the faults. These findings are however submitted to a very restrictive hypothesis: the fault system is globally critical, that is, close to a global loss of static equilibrium. Fault seismic activity is the signature that the system sometimes looses its static equilibrium but it is often very locally, at a nucleation point or in a collection of small seismic event. Because of this particularity of the model of Wolf *et al.* (2006), we will reexamine these questions with the present new quasi-static model of fault growth. As in Wolf *et al.* (2006), the present model is a 2-D elastic antiplane fault model with slip dependent friction. Although general problems with many faults can be studied by the method presented in this paper, we will only show results for a system of two parallel non-coplanar faults.

After Section 2 (physical assumptions of the model) and Section 3 (general definitions and notations), we present the quasi-static problem and several numerical experiments in Section 4. In Section 5, we reconsider the bifurcation of the spectral problem of Wolf *et al.* (2006) to interpret some particular features encountered in the quasi-static simulations, especially the effect of shadowing on stress intensity and the possible loss of global stability. In Section 6, we discuss the geometry and the stress field of relay zones, we show the effect of the interaction on fault tip velocities and on cohesive zones, and we discuss the relevance of our mechanical assumptions. Finally, some conclusions are drawn in Section 7. For clarity, most of the technical details concerning analytical and numerical methods are developed in appendices.

## 2 PHYSICAL ASSUMPTIONS OF THE QUASI-STATIC FAULTING MODEL

The rheological assumptions of the model are exposed here and will be discussed further in Section 6.3 in the light of our numerical results. The goal of this study is to model and quantify the effect of stress interaction in long-term quasi-static faulting process (fault growth and slip).

To begin with, the crust is considered elastic, and thus inelastic behaviour is only concentrated on faults. Fault growth is directly related to the increase of remote tectonic loading, hence we do not consider the possibility of sub-critical growth, at constant remote loading.

Regarding the failure criterion, there are several possible models based on either singular (asymptotic) stress or finite stress. Based on toughness or localized fracture energy, failure criteria with singular stress have the disadvantage that the mechanical behaviour of the intact crust (locally unlimited strength) is totally different from that of the faults (limited strength). Yamashita & Knopoff (1992) have used such kind of criterion in an earthquake clustering model, in which they model the growth and acceleration of parallel concurrent cracks. The large difference of mechanical behaviour between crust and fault is less justified at the tectonic timescale. In addition, stress singularities may strongly affect the state of stress in fault relays. For these reasons, we use a finite stress, slip-dependent, frictional behaviour. This failure criterion ensures both finite stress everywhere in the model and a progressive breakdown (that is, cohesive zones) at fault tips. Also, this failure criterion ensures quasi-static stability as long as the rate of mechanical work done by fault traction can balance the rate of released elastic potential energy. Usually, this condition is broken as the fracture length overcomes some critical value. However, stable fault growth rates can be achieved in different manners (like introducing stress relaxation, viscous relaxation or damage in the crust). Our model does not encompass such complexity, because it would introduce time dependence and new, poorly controlled, parameters. Rather, we impose an inhomogeneous strength excess, that depends on space and time. Strength excess is defined as the difference between the local shearing resistance (at zero slip) and the local shear loading. This quantity, which is mostly responsible for the growth of the faulting domain, can be defined arbitrarily in our model. Since the goal of the paper is to study the perturbative effects of fault interaction, we have to study also a reference model of isolated growing fault, as simple as possible. For example, as we will see further, to obtain a

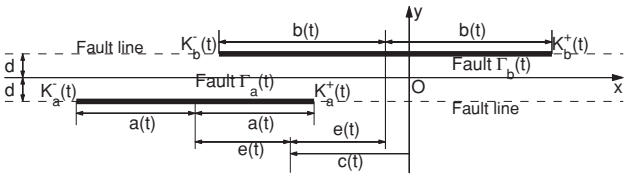


**Figure 1.** In the 2-D antiplane configuration, assuming an origin $O$ and two Cartesian coordinates $x$ and $y$, the geometry of two parallel straight but non planar faults is defined by the following parameters at each time $t$: variable fault lengths $2a(t)$ and $2b(t)$, fixed separation $2d$, variable offset $2e(t)$ and variable center $c(t)$. $K_a^-(t)$, $K_a^+(t)$, $K_b^-(t)$ and $K_b^+(t)$ are the stress intensity factors at the fault tips. $\Gamma_a(t)$ and $\Gamma_b(t)$ denote the slipping domains of faults. 'Fault lines' are the geometrical axes along which the faults are allowed to grow.

constant growth rate, it is enough to state that strength excess increases linearly in space starting from the nucleation point, and decreases linearly in time. In this way, in any fault network, the acceleration or deceleration of fault tips can be directly interpreted in terms of fault interaction.

## 3 GENERAL NOTATIONS

Let us define the main parameters used in the paper. The geometry of the two-fault system is drawn in Fig. 1. Variable $t$ denotes the time. $O$ is the origin of the axes and by $x$ and $y$ we denote the coordinates parallel and perpendicular to the fault direction. Parameters $a(t)$ and $b(t)$ are the variable fault half-lengths, $d$ is the fixed half-separation between faults (along $y$), $e(t)$ is the variable half-offset between the fault centres (along $x$) and $c(t)$ is the moving centre of the system (along $x$). We call 'fault lines' the geometrical axes along which the faults are allowed to grow. The slipping domains on each fault line are denoted $\Gamma_a(t)$ and $\Gamma_b(t)$. With these notations, we write the sets of points belonging to each slipping domain as

$$\Gamma_a(t) = \{(x, y);\ |x - c(t) + e(t)| < a(t),\ y = -d\}, \tag{1}$$

$$\Gamma_b(t) = \{(x, y);\ |x - c(t) - e(t)| < b(t),\ y = +d\}. \tag{2}$$

We will also use the following notations and equations for the different physical fields: displacement field (3), antiplane stresses (4), static equilibrium (5), slips on fault lines (6), slip velocities on fault lines (7) and elastic shear stress on fault lines (8)

$$w(t, x, y), \tag{3}$$

$$\begin{cases} \sigma(t, x, y) = \mu \partial_x w(t, x, y), \\ \tau(t, x, y) = \mu \partial_y w(t, x, y), \end{cases} \tag{4}$$

$$\partial_x \sigma(t, x, y) + \partial_y \tau(t, x, y) = 0, \tag{5}$$

$$\begin{cases} \delta w_a(t, x) = w(t, x, -d^+) - w(t, x, -d^-), \\ \delta w_b(t, x) = w(t, x, +d^+) - w(t, x, +d^-), \end{cases} \tag{6}$$

$$\begin{cases} \delta \dot{w}_a(t, x) = \partial_t \delta w_a(t, x), \\ \delta \dot{w}_b(t, x) = \partial_t \delta w_b(t, x), \end{cases} \tag{7}$$

$$\begin{cases} \tau_a(t, x) = \tau(t, x, -d), \\ \tau_b(t, x) = \tau(t, x, +d), \end{cases} \tag{8}$$

where $\mu$ is the shear elastic modulus.

As we will see hereafter, only the loading term is time dependent. Therefore, time variable $t$ is dropped in the appendices to simplify the equations. For the time-independent spectral problem in Section 5, time is dropped as well and $c$ will be set to zero without any loss of generality.

In Fig. 1, we have indicated the stress intensity factors at the fault tips, whose definitions are

$$K_a^-(t) = \lim_{x \to -a^-} \frac{\tau_a(t, x)}{\sqrt{-2\pi(x + a)}},$$

$$K_a^+(t) = \lim_{x \to +a^+} \frac{\tau_a(t, x)}{\sqrt{2\pi(x - a)}}$$

$$K_b^-(t) = \lim_{x \to -b^-} \frac{\tau_b(t, x)}{\sqrt{-2\pi(x + b)}},$$

$$K_b^+(t) = \lim_{x \to +b^+} \frac{\tau_b(t, x)}{\sqrt{2\pi(x - b)}}.$$

## 4 THE QUASI-STATIC PROBLEM OF TWO INTERACTING PARALLEL NON-COPLANAR FRICTIONAL FAULTS

### 4.1 Problem statement and numerical method

We consider the quasi-static non-linear problem of two interacting parallel frictional faults of fixed separation $2d$, that are allowed to slip and grow straightly along two fault lines, at $y = -d$ for the first fault and at $y = +d$ for the second one. In addition to the definitions and eqs (3)–(8), we denote by $\tau_a^l(t, x)$ and $\tau_b^l(t, x)$ the external tectonic loading acting on the fault lines at each time $t$. The resulting shear stress on both fault lines is the sum of the external tectonic loading and of the elastic shear stress created by the fault slips. The resistance along each fault line is given by a non-linear weakening frictional model that imposes the following conditions for all $t > 0$ and $x \in \mathbb{R}$:

$$\delta \dot{w}_a(t, x) = 0 \Rightarrow \quad \left|\tau_a(t, x) + \tau_a^l(t, x)\right| < \tau_a^f[x, \delta w_a(t, x)], \tag{9}$$

$$\delta \dot{w}_a(t, x) \neq 0 \Rightarrow \quad \tau_a(t, x) + \tau_a^l(t, x) = \text{sign}[\delta \dot{w}_a(t, x)] \tau_a^f[x, \delta w_a(t, x)], \tag{10}$$

$$\delta \dot{w}_b(t, x) = 0 \Rightarrow \quad \left|\tau_b(t, x) + \tau_b^l(t, x)\right| < \tau_b^f[x, \delta w_b(t, x)], \tag{11}$$

$$\delta \dot{w}_b(t, x) \neq 0 \Rightarrow \quad \tau_b(t, x) + \tau_b^l(t, x) = \text{sign}[\delta \dot{w}_b(t, x)] \tau_b^f[x, \delta w_b(t, x)], \tag{12}$$

where functions $\tau_a^f[x, \delta w_a(t, x)]$ and $\tau_b^f[x, \delta w_b(t, x)]$ are the local slip dependent frictions on each fault. The quasi-static problem is the problem defined by (3–8, 9–12).

Note that there is no intrinsic timescale in problem (3–8, 9–12) because of the elastic rheology and the removal of inertia. Time is only present in the external tectonic loading. The problem is purely quasi-static and therefore, to define a sliding velocity, one must obtain a smooth evolution of the system. This can be obtained by slowly and continuously increasing the time-dependent external tectonic loading. If the system admits a unique position of equilibrium after each increment of the external tectonic loading, the

evolution of the system should also be smooth enough. However, it is important to note that it is theoretically possible to find a position of equilibrium in one large time step, if the system admits a unique solution (which is verified if it has not lost its global convexity). We will not proceed with large time steps because it is much harder to find the solution from a 'bad' initial guess and also we could miss the first instants of the fault birth and growth, which we precisely want to study.

In the quasi-static problem, frictional conditions (9)–(12) constrain the slipping domain on both fault lines. The mathematical problem has already been solved for an isolated fault by Bonafede *et al.* (1985) and by Chen & Knopoff (1986). They studied this problem to find a static equilibrium after a rupture (the solution combines a prescribed stress drop in the fault and a finite strength at the edges of the rupture). In the context of earthquake nucleation studies, Uenishi & Rice (2003) solved this problem for a single isolated nucleation domain by modifying the frictional formulation into a stress intensity formulation. Let us shortly recall their method since we use it here. At any time $t$, slipping domains on both faults $\Gamma_a(t)$ and $\Gamma_b(t)$ are defined by (1) and (2). Each simulation starts with no existing fault, that is, (9) and (11) are verified everywhere and $a(0) = b(0) = 0$. As loading increases, the frictional threshold is reached at some places on both fault lines at time $t$. Consequently a slipping domain appears on both fault lines and we obtain two incipient faults of half-lengths $a(t)$ and $b(t)$, placed along $x$ according to parameters $c(t)$ and $e(t)$. On $\Gamma_a(t)$ and $\Gamma_b(t)$, (10) and (12) hold because slip occurs, whereas on the rest of the fault lines, where slip has not occurred, (9) and (11) must hold. However, since slip occurs on $\Gamma_a(t)$ and $\Gamma_b(t)$, shear stress accumulates at tips following the classical inverse square-root singularity. However stress cannot be singular at fault tips to satisfy (9) and (11), hence stress intensity factors at fault tips must be cancelled. We also consider that fault sliding velocities remain positive and therefore we can replace frictional conditions (9)–(12) by the following equations. For all time $t > 0$

$$\text{On } \Gamma_a(t):\ \tau_a(t,x) + \tau_a^l(t,x) = \tau_a^f[x, \delta w_a(t,x)], \tag{13}$$

$$\text{On } \Gamma_b(t):\ \tau_b(t,x) + \tau_b^l(t,x) = \tau_b^f[x, \delta w_b(t,x)], \tag{14}$$

$$K_a^+(t) = K_a^-(t) = K_b^+(t) = K_b^-(t) = 0. \tag{15}$$

Since the geometry of the faults [defined by the four variables $a(t)$, $b(t)$, $c(t)$ and $e(t)$] is unknown, the location of fault tips is constrained by the four eqs (15).

We emphasize that problems (3–8, 9–12) and (3–8, 13–15) are absolutely not equivalent in general. They become equivalent only 'in the cases where slip and fault lengths increase monotonically'. Thus, problem (3–8, 13–15) is a partly linearized version of problem (3–8, 9–12).

The technical aspects of the method are detailed in Appendices A, B and C. Roughly, we use truncated Chebyshev series to formulate the slipping functions on faults, following Dascalu *et al.* (2000):

$$\text{On } \Gamma_a(t):\ \delta w_a(t,x) = 2\sum_{k=1}^{N} W_{ak}(t) \sin\left\{k \arccos\left[\frac{x - c(t) + e(t)}{a(t)}\right]\right\}, \tag{16}$$

$$\text{On } \Gamma_b(t):\ \delta w_b(t,x) = 2\sum_{k=1}^{N} W_{bk}(t) \sin\left\{k \arccos\left[\frac{x - c(t) - e(t)}{b(t)}\right]\right\}. \tag{17}$$

This introduces $2N$ time-dependent scalars $W_{ak}(t)$ and $W_{bk}(t)$, that represent the series expansions of the fault slips at each time $t$. To formulate the frictional conditions on the faults, we need to know the elementary elastic solution in the 2-D elastic body for a single isolated fault and for a slipping function of index $k$. These elementary solutions are presented in Appendix A. The complete formulation of the series expansion is written in Appendix B. Then, following Uenishi & Rice (2003), eqs (13)–(15) are expressed in this series representation and for each time $t$ we find the $2N + 4$ scalars $W_{ak}(t)$, $W_{bk}(t)$, $a(t)$, $b(t)$, $e(t)$ and $c(t)$ by Newton's method (see Appendix C).

Let us now detail the loading and the frictional model. We assume that the crust, along each fault line, obeys to the following form of friction law, for all $x \in \mathbb{R}$

$$\tau_a^f(x, \delta w_a) = \tau_a^f(x, 0) - \alpha_a \frac{\delta w_a}{2} + \tau_a^r(\delta w_a), \tag{18}$$

$$\tau_b^f(x, \delta w_b) = \tau_b^f(x, 0) - \alpha_b \frac{\delta w_b}{2} + \tau_b^r(\delta w_b), \tag{19}$$

where $\tau_a^f(x, 0)$, $\tau_b^f(x, 0)$ are crust resistances along fault lines, $\alpha_a$, $\alpha_b$ their initial weakening rates and $\tau_a^r[\delta w_a(t, x)]$, $\tau_b^r[\delta w_b(t, x)]$ the non-linear part of the slip dependence of the friction. This decomposition leads to reformulate (13) and (14) as follows, for all $t > 0$

$$\text{On } \Gamma_a(t):\ \tau_a(t,x) = \tau_a^e(t,x) - \alpha_a \frac{\delta w_a(t,x)}{2} + \tau_a^r[\delta w_a(t,x)], \tag{20}$$

$$\text{On } \Gamma_b(t):\ \tau_b(t,x) = \tau_b^e(t,x) - \alpha_b \frac{\delta w_b(t,x)}{2} + \tau_b^r[\delta w_b(t,x)], \tag{21}$$

where $\tau_a^e(t,x) = \tau_a^f(x,0) - \tau_a^l(t,x)$ and $\tau_b^e(t,x) = \tau_b^f(x,0) - \tau_b^l(t,x)$ are the strength excesses of the crust along the fault lines. We will use the following particular idealized forms, for all $t > 0$ and for all $x \in \mathbb{R}$:

$$\tau_a^e(t,x) = -\gamma_a t + \delta_a \left[\sqrt{\epsilon_a^2 + \frac{(x + \xi_a)^2}{l_a^2}} - \epsilon_a\right], \tag{22}$$

$$\tau_b^e(t,x) = -\gamma_b t + \delta_b \left[\sqrt{\epsilon_b^2 + \frac{(x - \xi_b)^2}{l_b^2}} - \epsilon_b\right]. \tag{23}$$

As mentioned in Section 2, these ad hoc strength excesses variations with triangular shape have been chosen to produce a very simple (almost self-similar) faulting process for an isolated fault, with constant fault tip velocities. Furthermore, if fault weakening saturates early enough, this shape of strength excess ensures the existence of a long period of stable quasi-static regime. The functions defined by (22) and (23) are hyperbolic branches such that we obtain a global triangular shape, smoothed at the top by parameters $\epsilon_a$ and $\epsilon_b$. The smoothing is introduced only for numerical convenience, that is to avoid spurious spatial slip oscillations. Note that the opposite of the strength excess distributions can be directly observed, at time $t = 0$, in Fig. 3 (at right-hand side) and Fig. 4. The spatial slopes are controlled by $\delta_a/l_a$ and $\delta_b/l_b$ and the uniform rates of variation are controlled by $\gamma_a$ and $\gamma_b$. We remark that $\tau_a^e(0, -\xi_a) = 0$ and $\tau_b^e(0, \xi_b) = 0$, which means that at $t = 0$, the first fault arises at $(x = -\xi_a, y = -d)$ and the second one arises at $(x = \xi_b, y = d)$. Consequently, $c(0) = (\xi_b - \xi_a)/2$ and $e(0) = (\xi_a + \xi_b)/2$.

To finish with the definitions, the non-linear part of the slip dependence of the friction will be either set to zero in some experiments or defined by

$$\tau_a^r(\delta w_a) = \alpha_a \frac{\delta w_a}{2} + \Delta\tau_a \left[ \frac{1}{1 + \frac{\alpha_a D_a}{2\Delta\tau_a}\left(e^{\frac{\delta w_a}{D_a}} - 1\right)} - 1 \right], \qquad (24)$$

$$\tau_b^r(\delta w_b) = \alpha_b \frac{\delta w_b}{2} + \Delta\tau_b \left[ \frac{1}{1 + \frac{\alpha_b D_b}{2\Delta\tau_b}\left(e^{\frac{\delta w_b}{D_b}} - 1\right)} - 1 \right], \qquad (25)$$

in more realistic numerical experiments. In definitions (24) and (25), parameters $\Delta\tau_a$ and $\Delta\tau_b$ are the fault stress drops and $D_a$ and $D_b$ are characteristic slip weakening distances. Remark that $\tau_a^r(\delta w_a)$ and $\tau_b^r(\delta w_b)$ are the second order terms of the friction laws $\tau_a^f(x, \delta w_a)$ and $\tau_b^f(x, \delta w_b)$ as slips $\delta w_a$ and $\delta w_b$ go towards zero. Note also that for $D_a = \Delta\tau_a = \infty$ and $D_b = \Delta\tau_b = \infty$ we have $\tau_a^r(\delta w_a) = 0$ and $\tau_b^r(\delta w_b) = 0$. In addition, when $\alpha_a = \frac{2\Delta\tau_a}{D_a}$ and $\alpha_b = \frac{2\Delta\tau_b}{D_b}$, the non-linear terms $\tau_a^r$ and $\tau_b^r$ have an initial weakening rate that corresponds to the global characteristic weakening rate induced by the ratio of the stress drop to the critical slip weakening distance.

### 4.2 Numerical experiments for two faults with symmetric mechanical parameters

We conducted several sets of numerical experiments. First, let us present twelve characteristic symmetric simulations (here 'symmetric' means that both fault lines have the same frictional parameters and are subject to the same loading, which produces two equivalent faults). In these twelve experiments, we used four values of the half-separation $d$ combined to three different cases that differ qualitatively by their frictional parameters.

Case 1: $\alpha_a = \alpha_b = 0$ and $\tau_a^r = \tau_b^r = 0$, that is, fault slip is built at constant stress.

Case 2: $\tau_a^r = \tau_b^r = 0$, that is, faults are subject to constant weakening with $\alpha_a > 0$ and $\alpha_b > 0$.

Case 3: we use the complete frictional models defined in (18) and (19) with (24) and (25), therefore initial weakenings (controlled by $\alpha_a$ and $\alpha_b$) saturate asymptotically to finite stress drops $\Delta\tau_a$ and $\Delta\tau_b$, as slips go beyond the characteristic slips $D_a$ and $D_b$.

In all these experiments, we define the characteristic quantities of length, time, displacement and stress $\bar{l}$, $\bar{t}$, $\bar{w}$ and $\bar{\tau}$. Any combination of scales $\bar{l}$, $\bar{t}$, $\bar{w}$ and $\bar{\tau}$ is possible as soon as it respects the equalities $\bar{\tau} = \mu\frac{\bar{w}}{\bar{l}} = \frac{\gamma_a+\gamma_b}{2}\bar{t}$. In the twelve simulations, we start with the same $e(0)$, which is the initial half-distance along $x$ between the fault arising points. Therefore, $e(0) = (\xi_a + \xi_b)/2$ can be considered as the characteristic length scale $\bar{l}$. In Table 1, we give the value of all simulation parameters.

Before we compare these 12 simulations, let us examine in more detail three typical ones (4, 5 and 6) that share the same half-separation $d/\bar{l} = 0.1$. In Fig. 2, we show the slip processes on both faults for the simulation 4 (case 1). Here, no stress drop occurs and therefore the system remains indefinitely stable. At the beginning of the process, all fault tips have a constant speed of propagation and moreover their positions at time $t$ correspond roughly to the abscissa $x$ such that $\tau_a^e(t, x) = 0$ for fault $\Gamma_a(t)$ and $\tau_b^e(t, x) = 0$ for fault $\Gamma_b(t)$ (see definitions 22 and 23). As faults grow, stress interaction influences essentially the inner tips: first they accelerate and then they decelerate as the overlap grows, down to a stable slow speed of propagation.

**Table 1.** Parameters of the symmetric simulations.

| Simul. (Case) | $\frac{d}{\bar{l}}$ | $\alpha\bar{l}$ | $\frac{D}{\bar{w}}$ | Simul. (Case) | $\frac{d}{\bar{l}}$ | $\alpha\bar{l}$ | $\frac{D}{\bar{w}}$ |
|---|---|---|---|---|---|---|---|
| 1(1) | 0.02 | 0 | $+\infty$ | 7(1) | 0.5 | 0 | $+\infty$ |
| 2(2) | 0.02 | 0.1 | $+\infty$ | 8(2) | 0.5 | 0.1 | $+\infty$ |
| 3(3) | 0.02 | 0.1 | 10.0 | 9(3) | 0.5 | 0.1 | 10.0 |
| 4(1) | 0.1 | 0 | $+\infty$ | 10(1) | 2.5 | 0 | $+\infty$ |
| 5(2) | 0.1 | 0.1 | $+\infty$ | 11(2) | 2.5 | 0.1 | $+\infty$ |
| 6(3) | 0.1 | 0.1 | 10.0 | 12(3) | 2.5 | 0.1 | 10.0 |

| $\mu$ | $\gamma$ | $\frac{\delta}{\bar{\tau}}$ | $\epsilon$ (no dim.) | $\frac{\xi}{\bar{l}}$ | $\frac{l}{\bar{l}}$ | $N$ | $\frac{T}{\bar{t}}$ | $P$ |
|---|---|---|---|---|---|---|---|---|
| 1. | 0.025 | 1. | 0.2 | 1. | 1. | 80 | 200. | 200 |

*Notes:* All parameters are identical on both faults therefore subscripts $a$ and $b$ are omitted. When the critical slip weakening distance is set to infinity, faults have a constant weakening rate. Integer $N$ is the number of Chebyshev functions used, $T$ is the duration and $P$ is the number of steps to reach time $T$.
For all cases we choose

$$\Delta\tau = \frac{\alpha D}{2}.$$

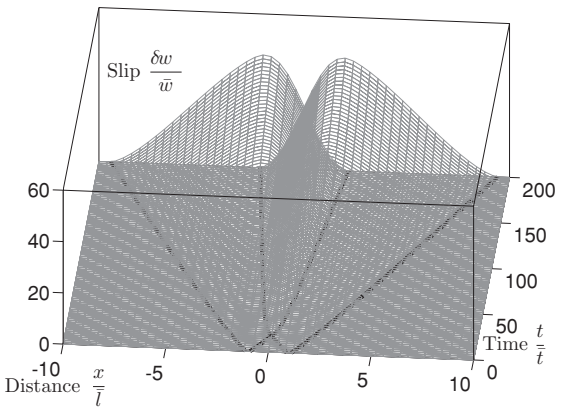


**Figure 2.** Quasi-static slip process for the symmetric simulation 4 (see Table 1). In this simulation, faults are subject to a constant strength, without weakening. We can see the strong deceleration of the inner tips propagation when faults overlap.

In Fig. 3, we represent the stress evolution for the same simulation 4 (case 1) in two manners: the elastic stress along faults lines due to fault slips and the 'relative stress' along faults lines. By 'relative stress', we mean either the difference between the elastic stress and the local fault line strength excess before slip occurs, or equivalently the difference between the total stress (loading + elastic stress) and the local fault line strength before slip occurs. This corresponds to the quantities $\tau_a(t, x) - \tau_a^e(t, x) = \tau_a(t, x) + \tau_a^l(t, x) - \tau_a^f(x, 0)$ and $\tau_b(t, x) - \tau_b^e(t, x) = \tau_b(t, x) + \tau_b^l(t, x) - \tau_b^f(x, 0)$. Since the model is only sensitive to the difference between the total stress and the fault line strength, absolute level of stress as well as absolute levels of friction are not relevant in this study. Therefore, this definition of 'relative stress' is needed to emphasize the difference between the different cases as defined earlier.

In Fig. 4, we represent the evolution of the relative stress for simulations 5 (case 2) and 6 (case 3). In simulation 5, a constant weakening is prescribed. At the beginning, fault tip propagation is similar as in simulation 4, only slightly faster. At the end of simulation 5, faults have reached a critical size that puts the system in a globally unstable configuration (equilibrium is lost), which is

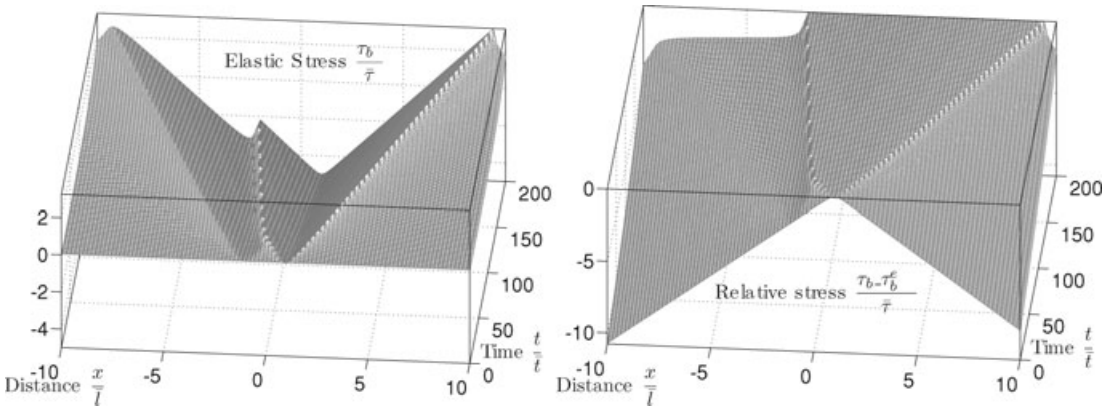


**Figure 3.** Quasi-static stress evolution for the symmetric simulation 4 (see Table 1). In this simulation, faults are subject to a constant strength, without weakening. We represent the stress evolution on the fault line of the second fault, that is, on $\Gamma_b$. More precisely: on the left-hand panel, we represent the elastic stress (due to the slip on both faults), and on the right-hand panel, we represent the 'relative stress', that is, the elastic stress minus the fault line strength excess, or equivalently the total stress (loading + elastic stress) minus the local fault line strength before slip occurs.

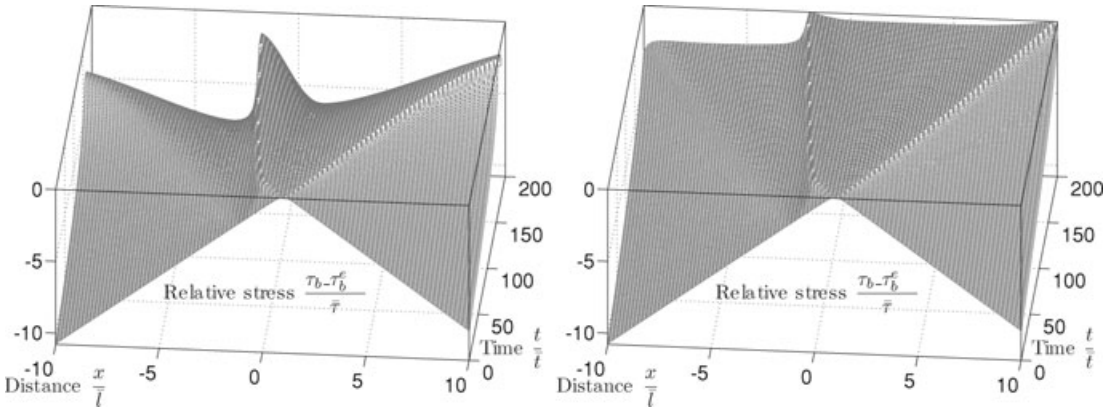


**Figure 4.** Quasi-static stress evolution for the symmetric simulations 5 and 6 (see Table 1). On both figures, we represent the same quantity as on Fig. 3 (right-hand panel), that is, the 'relative stress'. On the left-hand panel (simulation 5), weakening is strong and constant and we clearly see the continual stress decrease. On the right-hand panel (simulation 6), weakening ceases as the slip reaches $10\bar{w}$ and therefore we see the constant stress level inside the fault delimited by two cohesive zones.

theoretically predicted (Uenishi & Rice 2003). Before the instability occurs, outer tips accelerated strongly up to an infinite speed. For this reason, the computation was stopped at time $t = 179\bar{t}$. This global instability is not realistic and there are many features that can stabilize fault growth in nature; this is an important point that we will discuss further in Section 5.3. In simulation 6 (case 3), by introducing a critical weakening distance, the strong initial weakening is saturated far before the instability occurs. The relative stress exhibits cohesive zones at the fault tips and faults are maintained stable much longer. Fault tips seem to propagate very similarly as in simulation 4.

Finally, in Fig. 5, we summarize the results of the twelve symmetric simulations by plotting the fault tip locations, that is, their abscissa along $x$, as functions of time. We can observe the strong influence of a small initial separation $d/e(0)$ on the variation of the propagation speed of the inner (left-hand side) fault tip. Although the inner tip is never strictly stopped in all these symmetric simulations, its progression can be strongly affected as in simulations 1, 2 and 3.

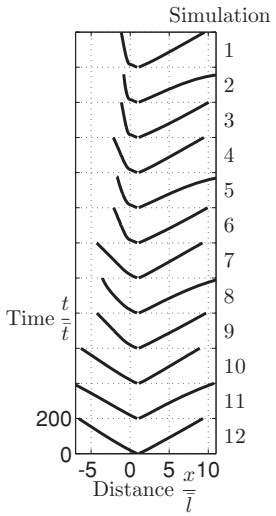


**Figure 5.** Evolution of fault tip locations for the twelve symmetric simulations (see Table 1). Only the tips of fault $\Gamma_b(t)$ are represented.

### 4.3 Numerical convergence

Since we solve each time step independently, the number of time steps has no effect on the accuracy of the numerical solution.

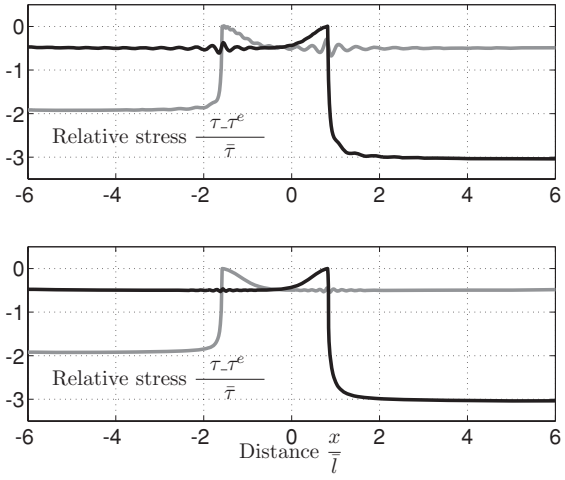


**Figure 6.** Convergence test for simulation 1. In this simulation, as faults overlap, the separation $d$ is small compared to fault sizes, therefore they interact strongly. On both figures we represent the relative stress at time $t = 200\bar{t}$. The number of modes used per fault is $N = 80$ at the top and $N = 160$ at the bottom. The shapes of the solutions are similar and the differences (spurious oscillations for $N = 80$) appear essentially on both faults in front of the overlapping tip, where stress admits strong variations.

Large time steps only increase the number of iterations of Newton's method since the first guess, based on the previous time step, is less good. The stopping criterion of Newton's method can reach the computer precision with little cost. The main source of error comes from the number $N$ of Chebyshev functions per fault, which can not be too large for computational reasons. However, this basis of functions is not only very accurate to estimate stress intensities but also very efficient to handle strong field variations at fault tips. Therefore, we performed the various simulations with only $N = 80$. However, we encountered situations where the results exhibit spurious oscillations. This occurs when strong field variations are induced inside the faults, that is, if $\tau_a^e(t, x)$ or $\tau_b^e(t, x)$ are not smooth enough, or if the cohesive zones are too small, or if faults are in strong interaction, which is what we illustrate in Fig. 6: in this case of small initial separation, $N = 160$ is patently more appropriate than $N = 80$.

### 4.4 Numerical experiments for two faults with non-symmetric mechanical parameters

In this section, we add a slight perturbation of the mechanical parameters to break the symmetry of the model. Indeed, perfect symmetry is never observed on natural fault systems. Besides, in the previous sections, we showed that most of the results could be explained through the strength excess distributions $\tau_a^e(t, x)$ and $\tau_b^e(t, x)$. Hence, we chose to use heterogeneous tectonic loading rates to introduce spatial dissymmetry. We define another set of twelve non-symmetric quasi-static simulations denoted $1'$ to $12'$. In these new simulations, the loading rate is slightly larger on fault line $\Gamma_b$, indeed

$$\gamma_a = 0.025 = \frac{9}{10}\gamma_b.$$

Note that the dissymmetry is rather small. The other parameters follow Table 1.

In Fig. 7, we illustrate the slip process for simulation $6'$, that includes broken symmetry, non-linear slip weakening, and strength saturation. The global behaviour is very similar to simulation 4,

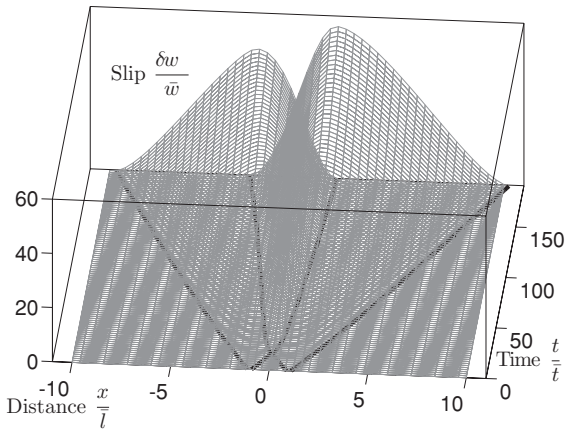


**Figure 7.** Quasi-static slip process for the non-symmetric simulation $6'$ (see Table 1). In this simulation, faults are subject to a variable strength, that decreases non-linearly with slip and saturates at a dimensionless value of 5.

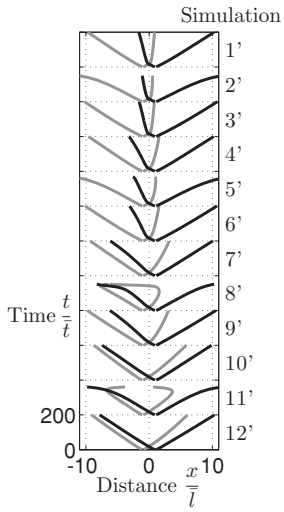


**Figure 8.** Evolution of fault tip locations for the twelve non-symmetric simulations. Parameters follow Table 1, with the only difference that the loading rate is slightly larger on the fault line $\Gamma_b(t)$, indeed $\gamma_a = 0.025 = \frac{9}{10}\gamma_b$. Black lines correspond to the tips of the 'dominant' fault $\Gamma_b(t)$ and grey lines correspond to the tips of the dominated fault $\Gamma_a(t)$.

except that faults show differences of both maximal slips and tip locations (due to slightly different loading rates). Because of slip weakening, this dissymmetry amplifies progressively and is particularly remarkable at the end of the simulation.

In Fig. 8, we represent the fault tip trajectories. The first remark that can be done is that, in all the simulations, as overlap appears, the inner tip of the slowest fault $\Gamma_a(t)$ is much more decelerated than the one of $\Gamma_b(t)$. Therefore, the lack of symmetry is amplified in time. The influence of the initial separation $d/e(0)$ is roughly the same as in symmetric simulations: a small initial separation $d/e(0)$ induces a strong deceleration of inner fault tips.

The second remark concerns simulations of case 2 ($2'$, $5'$, $8'$ and $11'$). Here, weakening is strong and constant and a global instability occurs rapidly. Before the instability (equilibrium loss) is reached, the inner tip of the slowest fault propagates back, that is, the slipping zone is shrinking. For simulations $8'$ and $11'$, the large initial separation $d/e(0)$ induces a global shadow effect of the dominant fault $\Gamma_b(t)$ on the other one, such that the fault $\Gamma_b(t)$ accelerates bilaterally and totally inhibits fault $\Gamma_a(t)$. Both tips of the dominated

fault $\Gamma_a(t)$ propagate back and the fault literally disappears. Of course, if the absolute level of stress is high, the back-propagation of fault tips, as well as negative slip velocities, are prohibited in the quasi-static problem (3–8, 9–12). However, as we explained in Section 4.1, we solve problem (3–8, 13–15) instead, so that we can sometimes face this non-physical situation. Indeed, problem (3–8, 13–15) is 'less' non-linear than problem (3–8, 9–12) and they are only equivalent if the evolution of the system remains monotonic. This set of simulations illustrates that a lasting weakening process can lead to a total inhibition of an inner tip in a fault network. This will be explained in Section 5 through a spectral analysis. To conclude about the plausibility of simulations of case 2, we must recall the assumptions of the model: first, faults do not branch, that is, the relay zone is said 'open'; second, the stability of the fault network is close to critical, that is, the global equilibrium will be lost soon, for a modest load increment.

## 5 SPECTRAL ANALYSIS OF TWO INTERACTING FRICTIONAL FAULTS: EFFECT OF STRESS SHADOWING ON TIP STRESS INTENSITIES

In the previous section, we have illustrated the effect of stress interaction in the quasi-static faulting model. The effect is greater when the weakening process is important and critical. We have pointed out that one could observe the stopping (and reversing) of the straight propagation of the inner tip belonging to the dominated fault when the pair of faults is not symmetrically loaded. All these features can be explained by a spectral analysis. In this section, the equations are time-independent, therefore variable $t$ is dropped implicitly when using the definitions of Section 3. Let us recall that the modes found in the spectral analysis have in general no direct physical interpretation and only a summation of them can lead to a complete solution, such as the quasi-static solutions. However, in general, the first mode is dominant and thus sufficient to discuss real physical model.

### 5.1 Linear spectral analysis

For a given fault network geometry with fixed parameter $a$, $b$, $c$, $d$ and $e$, the linear spectral problem consists in finding solutions of (3)–(8) for which the elastic stress is proportional to the slip, that is,

$$\text{On } \Gamma_a\text{: } \tau_a(x) = -\alpha \frac{\delta w_a(x)}{2} \tag{26}$$

$$\text{On } \Gamma_b\text{: } \tau_b(x) = -\alpha \frac{\delta w_b(x)}{2}, \tag{27}$$

where $\alpha$ is the eigenvalue, which can be interpreted as a weakening parameter.

This linear spectral problem (3–8, 26, 27) is solved using the same fault slip Chebyshev series expansions as in Section 4 and the technical details are presented in Appendix D. The problem that we solve here is invariant by translation, thus we set $c = 0$. Furthermore, it can be rescaled by any length describing the fault network geometry, thus we set $a = 1$. We considered problem (3–8, 26, 27) for any triplet $(e, d, b) \in ]0, 0.9] \times ]0, 3] \times [0.05, 1[$. To explore this parameter space, we computed 65 540 solutions with a refinement of the exploration domain for small values of separation $2d$. The last important technical issue concerns the number of Chebyshev slip functions used for each of the 65 540 linear eigenvalue problems.

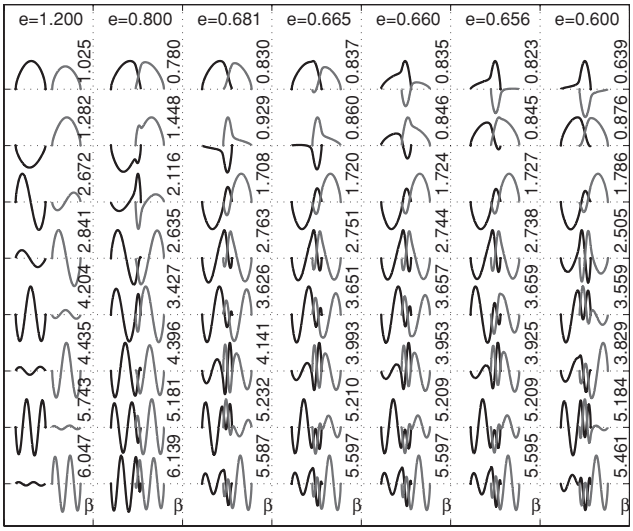


**Figure 9.** Seven examples of modes obtained by the linear spectral analysis. Here $a = 1$, $b = 0.95$ and $d = 0.03$. From left- to right-hand side the fault separation $e$ ranges progressively from a large value $e = 1.2$ (without overlap), to a smaller values $e = 0.6$ with significant overlap. In each column we plot the first eight eigenfunctions with their corresponding dimensionless eigenvalue $\beta$. Modes are normalized to amplitude 1. Slip on the largest fault $\Gamma_a$ (on the left-hand side) is drawn in black and slip on the smallest fault $\Gamma_b$ (on the right-hand side) is drawn is grey. The different values of $e$ have been chosen to show different situations due to the stress interaction.

For large values of the separation $2d$, the distance between fault tips is large, such that the interaction does not induce strong slip variations; consequently we used less than 50 Chebyshev slip functions per fault. In return, for small values of the separation $2d$, we used up to 200 Chebyshev slip functions per fault to handle the strong local variations. Finally, we introduce a natural dimensionless eigenvalue $\beta = \frac{\alpha}{\mu}\sqrt{ab}$ (see Appendix D).

In Fig. 9, we plot the results of the spectral analysis for seven geometries of different separations $e$, the other parameters being fixed to $a = 1$, $b = 0.95$ and $d = 0.03$. In the first column ($e = 1.2$), faults do not overlap and results are simple to interpret: the first mode gives slips of same sign and the second one shows opposite signs; for high order modes, the interaction of the faults decreases and the slip profiles tend to reproduce the simple Chebyshev functions alternatively on the faults. As fault begin to overlap (second column, $e = 0.8$), we see that the interaction increases for the higher order modes. On the first mode, quasi-linear segments of slip profile are present in the region of overlap. For $e = 0.681$, we encounter a critical point: the stress intensity of the first mode vanishes at the inner tip of the smallest fault $\Gamma_b$, that is $K_b^- \approx 0$. For $e = 0.665$, on the first mode, a small portion of negative slip arises on the left-hand side of the smallest fault $\Gamma_b$. For $e = 0.660$, the zone of negative slip on the first mode spreads and we have a second critical point in the sense that the eigenvalues of the two first modes $\beta_1$ and $\beta_2$ are very close (but not identical since there is no degeneration because the fault have different size). For $e = 0.656$, fault $\Gamma_b$ reaches the third critical point where the slip of the first mode becomes negative everywhere on $\Gamma_b$; furthermore the second mode has positive slip almost everywhere on both faults. Finally, for $e = 0.6$ we observe the stressing of the situation described for $e = 0.656$. To summarize, we see that the first mode provides a basic picture of fault interaction. As the fault overlap increases, in most cases, we observe the increasing

effect of the shadowing on the smallest fault (the weak fault), passing through three critical points such that 'on the first mode' we have

(1) Before the first critical point: $\delta w_a(x) > 0$ and $\delta w_b(x) > 0$.
(2) At the first critical point: $K_b^- = 0$.
(3) after the first critical point: $K_b^- < 0$ and $\delta w_b(x)$ is not positive everywhere on $\Gamma_b$.
(4) At the second critical point: $|\beta_1 - \beta_2|$ is minimal.
(5) At the third critical point: $\delta w_b(x) \leq 0$.
(6) After the third critical point: $\delta w_b(x) < 0$.

For the case $a = b$, we observed that the three critical points merge in a unique one, with an abrupt transition: the sign of the slip on one of the faults changes globally and we have $\beta_1 = \beta_2$ (degenerate system).

In the general case, it turns out that the first linear mode is not always suitable to describe a real physical problem. Indeed if the geometry has passed the first critical point ($K_b^- < 0$), the first mode bifurcates and does not respect the condition of slip positivity everywhere on the faults, which is a mandatory condition to respect a Coulomb-based frictional condition. This bifurcation depends on the geometry and assuming $a = 1$, it should link the geometrical parameters $e$, $d$ and $b$.

### 5.2 Bifurcation of the linear spectral problem: link with the Wolf *et al.* (2006) non linear spectral analysis

In this section, we determine the location of the bifurcation of the first slipping mode obtained by the linear spectral analysis and we compare our results with the non-linear spectral analysis of Wolf *et al.* (2006). We keep $a = 1$ without any loss of generality. In Section 5.1, we solved the linear spectral problem (3–8, 26, 27) for any triplet $(e, d, b) \in ]0, 0.9] \times ]0, 3] \times [0.05, 1[$. We found that the first mode could not respect slip positivity on the smallest fault, as soon as the stress intensity factor at its inner fault tip is negative. We define $\mathcal{K} = K_a^+ K_a^- K_b^+ K_b^-$ the product of all the stress intensity factors, and thus the bifurcation that we want to determine is located at $\mathcal{K} = 0$. By $S_{\mathcal{K}=0}$, we define the 2-D surface of the bifurcation in the 3-D parameter space $(e, d, b)$. Technically, since we have chosen $b < a$ and $e > 0$, condition $\mathcal{K} = 0$ reduces to $K_b^- = 0$; we have already remarked that for fixed value of $b$ and $d$, $K_b^-$ decreases continuously as $e$ decreases, reaches zero and finally becomes negative; thus we simply tracked this change of sign to extract the solutions for which $K_b^- = 0$ holds. The uncertainty of the results depends on the refinement of the exploration of the domain $(e, d, b) \in ]0, 0.9] \times ]0, 3] \times [0.05, 1[$. The surface of bifurcation $S_{\mathcal{K}=0}$ is drawn in gray in Fig. 10.

Ionescu & Wolf (2005) and Wolf *et al.* (2006) developed a finite element based technique to compute, on any arbitrary antiplane fault system, an eigenmode that respects the positivity of slip everywhere. We will not rewrite the problem statement but we will only recall the main assumptions. First, the slipping domain is partly unknown and only a 'potential' slipping domain is defined along geometrical segments. This makes possible to find an suitable faulting domain for which the positivity of slip and the stress finiteness is possible. Second, the problem is non-linear and it is not possible to reduce the spectral problem to a simple matrix eigenvalue search. Instead, only one fundamental mode is searched iteratively to minimize the eigenvalue (and to maximize the true slipping domain as they could observe). Depending on the geometrical parameters, they observe that the true slipping domain is either equal to or smaller than the potential slipping domain. When it is equal, the stress field is singular at fault tips and the non-linear mode turns into a classical linear mode. When it is smaller, which occurs as fault overlap enough, the smallest fault exhibits a locked zone (an inhibited section) in the shadow of the other fault. Therefore, the end of the true slipping domain is governed by friction and not by a barrier, and thus the stress field is not singular at the end of the true slipping domain. Consequently the non-linear fundamental modes of Wolf *et al.* (2006) must lie on the surface $S_{\mathcal{K}=0}$. To verify this, we used the finite element code of Ionescu & Wolf (2005) and computed 29 solutions of these non-linear spectral problems for two parallel non-coplanar faults. For each simulation we ensured that the problem was really non-linear and we measured the true slipping domain on the faults in order to extract parameters $a$, $b$ and $e$. In Fig. 10, we reported these points (white balls) and we verified successfully that they all lie on the surface $S_{\mathcal{K}=0}$ for a very wide range of configurations. In this way, we show that for two parallel non-coplanar antiplane faults, the surface $S_{\mathcal{K}=0}$ can be seen as the bifurcation of the linear spectral problem into a non-linear one.

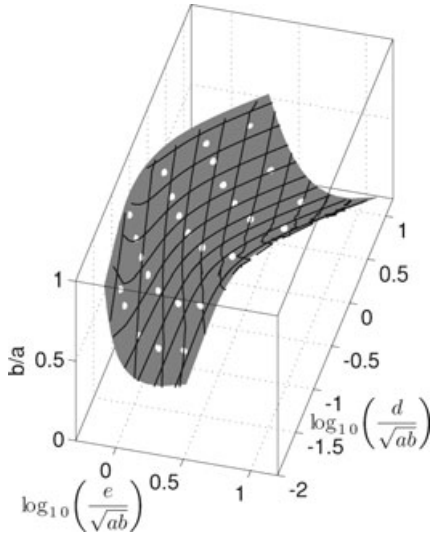


**Figure 10.** The grey surface represents the location of $S_{\mathcal{K}=0}$. The white balls represent the location of 29 solutions of the non-linear spectral problem as defined by Ionescu & Wolf (2005), that exhibit an inhibited fault segment. Geometrical parameters $a$, $b$, $d$ and $e$ are defined on Fig. 1; $b$ denotes the active length of the inhibited fault (that is, $g$ in the paper of Wolf *et al.* (2006)). The first (mainly horizontal) family of curves represents the $iso - \beta$ curves with $\beta = \frac{\alpha}{\mu}\sqrt{ab}$. As $b/a$ increases, the curves sample the iso-values 0.3, 0.4, 0.5, 0.6, 0.7, 0.8, 0.9, 1.0, 1.1. The second family of curves (quasi vertical curves) represents the iso-curves of the ratio of the maximum of slip on the smallest fault to the one on the largest one. As $d/\sqrt{ab}$ increases, these curves sample the iso-values $10^{-0.1}$, $10^{-0.5}$, $10^{-1}$, $10^{-1.5}$, $10^{-2}$, $10^{-2.5}$, $10^{-3}$, $10^{-3.5}$, $10^{-4}$, $10^{-4.5}$, $10^{-5}$.

In addition, we have drawn in Fig. 10 two families of curves that characterize the bifurcation. The first family of curves (quasi horizontal curves), corresponds to the $iso - \beta$ curves, where $\beta$ varies linearly from 0.3 for the lowest curve (small $b/a$) to 1.1 for the highest one (large $b/a$). The second family of curves (quasi vertical curves) represent the iso-values of the ratio of the maximum slip on the smallest fault to the one on the largest one. This ratio varies exponentially from 0.794 for small values of separation $2d$ to $10^{-5}$ for large values. This second family of curves illustrates a key effect in the bifurcation of the non-linear spectral problem: when faults are quasi coplanar (that is, for small values of $2d$) and as the offset $2e$ decreases, stress shadowing occurs strongly at inner fault tips, and therefore the signature of the bifurcation occurs 'locally'

at one fault tip by the cancellation of the stress intensity factor. By contrast, when faults are distant (that is, for large values of $2d$) and as the offset $2e$ decreases, stress shadowing occurs 'globally' and the slip on the smallest fault vanishes at the bifurcation. This situation must be commented since there exists distant parallel active faults with comparable importance: in this case stress shadowing is very weak and, very likely, tectonic loading and strength distribution (see the quasi-static model in Section 4) play a more important role in faulting processes than stress interaction.

### 5.3 Link between the loss of equilibrium of the quasi-static problem and the spectral analysis

In general, quasi-static fracture models based on a stress weakening process may be unstable for some loading conditions. For our particular quasi-static simulations with constant weakening (case 2), we observe the instability and we can explain it simply on the basis of the spectral analysis. This has already been studied in the context of dynamic slip nucleation. Following Dascalu *et al.* (2000) for an isolated fault, the static linear spectral computation determines the critical weakening that discriminates whether a small elastodynamic slip perturbation will induce an instability or not. More precisely, the instability occurs for a weakening larger than the critical weakening (the first eigenvalue). By investigating non co-planar fault dynamics, Ionescu & Wolf (2005) showed that for two non-coplanar parallel fault segments that overlap, the non-linear spectral computation is needed to handle correctly the frictional problem under stress shadowing interaction. Finally, following Uenishi & Rice (2003), for an isolated quasi-static slip process regularized at edges (like our model, theirs shows no stress singularity), the spectral analysis determines the critical length of a nucleation patch for a given weakening rate, for any shape of loading. All these studies, although conducted in a different context (rupture nucleation), can be used here to analyse the stability of our quasi-static problem.

The question we try to answer here is: what is the dominant sliding mode of the quasi-static system as it looses its equilibrium? We investigated this question numerically in the following manner: we compared the 'slip velocity' profiles of the quasi-static solution, 'at the global instability onset', with linear and non-linear eigenmodes computed with the final geometry of the fault system (at instability onset). Technically, the 'slip velocity' of the quasi-static simulation is deduced from the difference between the last two iterations (we had to refine the time step for this) and thus we inject the final geometry (i.e. the values of $a$, $b$, $d$ and $e$) in the computation of the linear and non-linear first modes. As it is shown in Fig. 11, for a quasi-symmetric loading situation, the first linear eigenfunction fits the sliding velocity of the quasi-static solution and the first linear eigenvalue corresponds to the uniform weakening used in the quasi-static computation, that is, $0.1/\bar{l}$. Furthermore, in this case, the first non-linear mode computed with the finite element code of Ionescu & Wolf (2005) is identical, that is, it does not contain any locked zone (the non-linear mode is equivalent to the linear one). By contrast, for a strongly non-symmetric loading, only the first linear mode seems to correspond to the sliding velocity and we clearly observe the back-slip on the dominated fault. Note that the back-slip is associated with the large slip velocity near the inner tip of the dominant fault. As expected, the non-linear eigenmode exhibits a locked zone in this strongly non-symmetric configuration. To conclude, at the onset of the loss of equilibrium, the slipping velocity of our partly linearized quasi-static problem (3–8, 13–15), which allows back-slip, is governed by the first *linear* mode (not the non-linear one). By analogy, we conjecture that the loss of equilibrium for the fully non-linear quasi-static problem (3–8, 9–12), which does not allow back-slip by definition, could be analyzed with the non-linear eigenmode analysis.

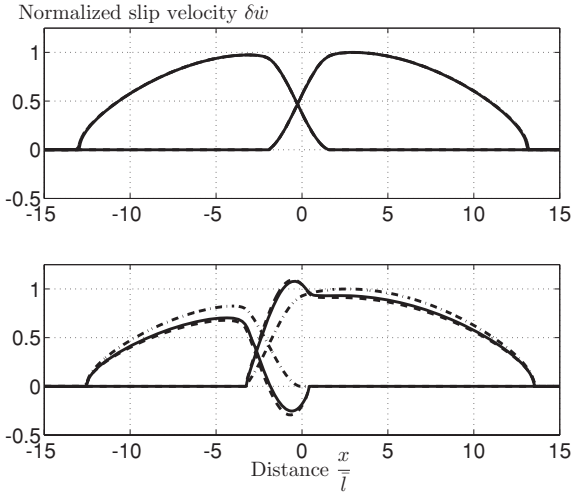


**Figure 11.** Comparison of quasi-static 'slip velocity' profiles at the global instability onset with eigenmodes. From top to bottom, solid lines represent quasi-static slip velocity profiles of one quasi-symmetric simulation $5''$ and one strongly non-symmetric simulation $5'''$. Simulations $5''$ and $5'''$ are similar to simulation $5'$ and differ only in their asymmetry of loading rate, that is, $\gamma_b/\gamma_a = 10/9.75$ and $10/8.6$, respectively. At the onset of instability, the geometry of the network is used to compute the linear eigenmodes with our Chebyshev method (dashed lines) and the non-linear eigenmodes with the finite element method of Ionescu & Wolf (2005) (dash–dotted lines). To facilitate the comparison, all profiles have been normalized around unity to minimize their differences of amplitude. Linear eigenvalues are, respectively, $0.1011/\bar{l}$ (for $5''$) and $0.1016/\bar{l}$ (for $5'''$). Non-linear eigenvalues are, respectively, $0.1012/\bar{l}$ (for $5''$) and $0.1226/\bar{l}$ (for $5'''$). For simulation $5''$, all curves are identical and all eigenvalues are equal to the quasi-static weakening (0.1) at 1 per cent confidence. For simulation $5'''$, only the non-linear eigenmode differs, and this is due to the back-slip process occurring in the partly linearized quasi-static problem (3–8), (13)–(15).

## 6 DISCUSSION

Here, we discuss several implications of our models to interpret some natural observations. First, we compare our results with the study of normal fault relays of metric size, done by Soliva & Benedicto (2004). Then we point out shortly the influence of fault interaction on fault tip velocities and on cohesive zones. To finish, we discuss the mechanical assumptions of the model.

### 6.1 Geometry and stress field of open relay zones

Many relays of normal faults of different sizes have been studied and classified by Soliva & Benedicto (2004). Especially, they studied slip distributions and geometrical characteristics of normal fault relays at different stages: 'open', 'linked' and 'fully breached'. 'Open relays' have no or few secondary faulting in the relay zone. 'Linked relays' have new faults that link the major faults (the process of coalescence has started). In 'fully breached' relays the faults are completely merged in one unique continuous fault and only a residual geometrical irregularity on the fault recalls the past existence of two independent faults. In this section, we try to interpret their results for open relays by means of both our spectral analysis and our

quasi-static numerical simulations. For linked and fully breached relays, a deeper comparison can not be conducted yet, since our quasi-static model needs improvements to account for fault linking processes by 'connecting' faults of different orientations. One of the key observations of Soliva & Benedicto (2004) is the mean ratio of fault separation to fault offset observed for each kind of relay (open, linked and fully breached). Experimentally, the geometry obeys the 'pre-linkage' rule $r \lesssim 2.9d$ for open relays, the 'in-linkage' rule $2.9d \lesssim r \lesssim 4.5d$ for linked relays and the 'post-linkage' rule $4.5d \lesssim r \lesssim 6d$ for fully breached relays, where $r = (b + a)/2 - e$ is the half-overlap of faults. To simplify the analysis, we will simply call $r \gtrsim 2.9d$ the 'linkage' rule. Note that these observed geometrical rules do not take into account the fault lengths $2a$ and $2b$: they are supposed to be valid for fault systems with small ratios of separation and overlap compared to fault lengths.

Let us begin with the spectral problem of two faults studied in Section 5. Because the modes take into account stress interaction and because the first mode should be dominant in slipping processes, it may reproduce partly the slip profiles encountered in real fault systems, especially in the relay zone, as Wolf *et al.* (2006) showed on a real fault system in Afar. The main result of the spectral analysis is the set $S_{\mathcal{K}=0}$ of critical geometries for which the stress intensity vanishes at one of the inner fault tips. The set $S_{\mathcal{K}=0}$ is a surface that links the parameters $b/a$, $d$ and $e$ together. Let us now argue, as Wolf *et al.* (2006), that on $S_{\mathcal{K}=0}$, a system of two faults subject to weakening has an inner fault tip that would not propagate straight because the stress intensity factor is zero; thus the linkage through secondary faulting should be preferred to the straight propagation of one fault in the shadow of the other. To check if this purely geometrical '$S_{\mathcal{K}=0}$ criterion' can be used to discriminate whether a relay is in the linkage process, we plot in Fig. 12 the points belonging to $S_{\mathcal{K}=0}$ and the boundary of the experimental linkage criterion (black thick line). First, let us remark that many points of $S_{\mathcal{K}=0}$ correspond to negative overlap and are out of the range of the data, but still, $S_{\mathcal{K}=0}$ (white circles) lies on a much larger area than the linkage region $r \gtrsim 2.9d$. Let us now restrict the points of $S_{\mathcal{K}=0}$, with an additional constraint of aspect ratio $b > 7.5d$ (black circles), to account for the criterion of small ratio $d/\min(a, b)$ that Soliva & Benedicto (2004) considered in their experimental study. With this additional constraint, we find a clear correlation between the experimental linkage criterion $r \gtrsim 2.9d$ and our '$S_{\mathcal{K}=0}$ criterion'. Note that this correlation disappears for very small values of separation.

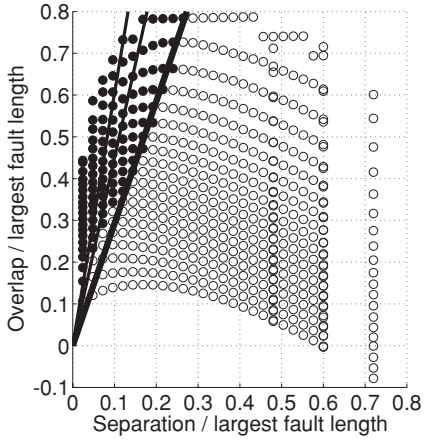


**Figure 12.** Locations of the points defining $S_{\mathcal{K}=0}$ compared to experimental data. The overlap $2r = (b + a) - 2e$ is plotted against the separation $2d$, both renormalized by the largest fault length $2a$. Following Soliva & Benedicto (2004), the thick solid line represents the best-fitting linear trend for open relays ($r \simeq 2.9d$). The other two solid lines represent the best-fitting linear trends of 'linked' and 'fully breached' relays. Each circle represents a point belonging to $S_{\mathcal{K}=0}$. The subset of $S_{\mathcal{K}=0}$ corresponding to the aspect ratio constraint $b > 7.5d$ is highlighted by means of black circles.

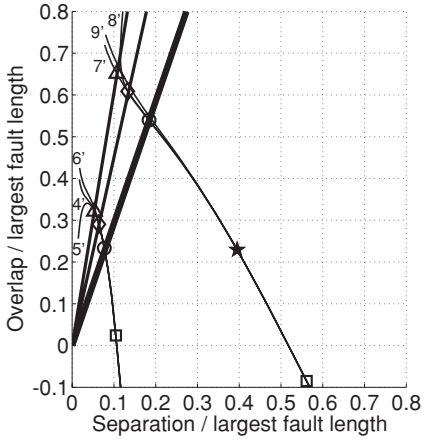


**Figure 13.** Paths of the quasi-static simulations $4'$, $5'$, $6'$, $7'$, $8'$ and $9'$ in the frame $r(t)/a(t)$ (normalized overlap) versus $d(t)/a(t)$ (normalized fault separation). The different symbols (squares, star, circles, diamonds and triangles) correspond to particular times where all simulations share a common characteristic. They are reported in time on Fig. 14. Circles, diamonds and triangles correspond to the intersection with experimental geometrical linkage criteria $r = 2.9d$, $r = 4.5d$ and $r = 6d$ from Soliva & Benedicto (2004), but only the first three simulations can really be compared to their results.

Now, we will comment the different stages of two sets of quasi-static numerical simulations. The first set of simulations $4'$, $5'$ and $6'$ with a small initial separation $d/e(0) = 0.1$ and a strong fault interaction will be interpreted in the light of the experimental observations of Soliva & Benedicto (2004). The second set of simulations $7'$, $8'$ and $9'$ has a large initial separation $d/e(0) = 0.5$, thus few fault interaction. Because of this large initial separation, it cannot be compared to their observations. However, the results for the second set are interesting as well, and for simplicity the results for both sets are presented on the same figures in order to ease comparisons. Because of the asymmetry, the bottom fault $\Gamma_a(t)$ will be called the dominated fault and the top fault $\Gamma_b(t)$ will be called the dominant one. In Fig. 13, we represent the paths followed by the quasi-static simulations in the frame of Fig. 12, that is, overlap $2r(t)$ against separation $2d$ (both normalized by the largest fault length $2a(t)$). Meanwhile, in Fig. 14 we represent, as functions of time, the fault tip velocities corresponding to the same quasi-static simulations. Furthermore we point with different symbols five particular times; the first two correspond to some particular moments in the simulations, and the last three correspond to the geometrical criterions of Soliva & Benedicto (2004) about linkage:

□: propagation speed of inner fault tips is maximal (excluding the fault birth),

★ (only for simulations $7'$, $8'$ and $9'$): faults begin to overlap,

◯: the fault system enters the experimental linkage zone ($r \gtrsim 2.9d$),

◇: the fault system enters the experimental post-linkage zone ($r \gtrsim 4.5d$),

△: the fault system passes $r \gtrsim 6d$, where only fully breached relays are observed.

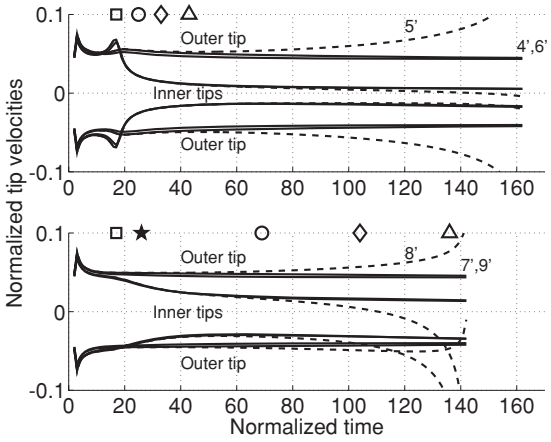


**Figure 14.** Fault tip velocities (normalized by $\bar{l}/\bar{t}$) as functions of the normalized time $t/\bar{t}$ for the quasi-static simulations 4′, 5′ and 6′ (top panel) and simulations 7′, 8′ and 9′ (bottom panel). Dotted lines correspond to simulations 5′ and 8′ with constant fault weakening. The different symbols (squares, star, circles, diamonds and triangles) correspond to particular times where all simulations share a common characteristic. The fault birth episode can be observed for $t/\bar{t} \leq 5$ in each simulation; note that it comes with large initial fault tip velocities.

In addition, at these particular times, we plot in Figs 15 and 16 the corresponding snapshots of the state of elastic shear stress for both sets of simulations (except simulations 4′ and 7′ that have no frictional weakening). More precisely, each picture represents an unsigned vector field which takes the orientation of the most sheared plane and the amplitude of the corresponding shear. This field is plotted only at places where the stress field would theoretically favour secondary faulting (that is, where the shear along $x$ is positive). Since we do not know the regional state of stress (pre-stress), we cannot compute the total stress; consequently, the conclusion that we can draw from these elastic shear stress pictures must be considered carefully regarding secondary faulting prediction.

Let us now describe the first set of simulations (4′, 5′ and 6′), which can be compared with the observations of Soliva & Benedicto (2004) through Figs 13, 14 and 15. At the instant pointed by squares, the overlap of faults is close to zero and fault tip velocities are maximal; also, at any point in the neighbourhood of the inner fault tips or inside the starting relay ramp, the most sheared plane is approximately oriented along tilted vector $(1, -1)$ . At this moment, it is reasonable to argue that faults are about to propagate in a new direction out of the relay (faults repulse each other). This is commonly observed on real fault relays. Here, it seems that the dominated fault is more concerned by this repulsion. In addition, secondary faulting may appear along this tilted direction. At the instant pointed by circles, faults overlap significantly and fault tip velocities are strongly reduced, but the state of stress looks similar (slightly more vertical inside the relay ramp). It is interesting to note that this time corresponds to the end of the strong deceleration of the inner fault tips (see Fig. 14). Afterwards, at times pointed by diamonds and triangles, the state of stress favouring secondary fractures shrinks to small regions in the vicinity of the fault tips. We can suppose that the active linking process is completed at the diamond. At the time pointed by triangles, the use of different friction laws does not really make a difference between simulations 5′ and 6′, indeed, these simulations are strongly controlled by the distribution of strength excess along fault lines.

Now we comment shortly the results for simulations 8′ and 9′ (see Figs 13, 14 and 16), compared to simulations 5′ and 6′ that we have just analyzed. At the times pointed by squares, the situations are qualitatively similar. The snapshots corresponding to stars for simulations 8′ and 9′ (Fig. 16) are comparable to those pointed by circles for 5′ and 6′ (Fig. 15). Preferred secondary fracturing is more vertical. At larger times (circles and diamonds), the state of stress favouring secondary fractures shrinks to small regions in the vicinity of the fault tips. Finally, in the last snapshots (triangles), the inner fault tip of the dominated fault is completely in the shadow and it even propagates back in simulation 8′. The inner fault tip of the dominant fault interacts with the outer tip of the dominated one (interaction is stronger in simulation 8′ because constant weakening amplifies the asymmetry of slip partition between the faults). In the last snapshot (triangle), simulation 8′ is close to the loss of equilibrium and this explains the difference with 9′ (this difference

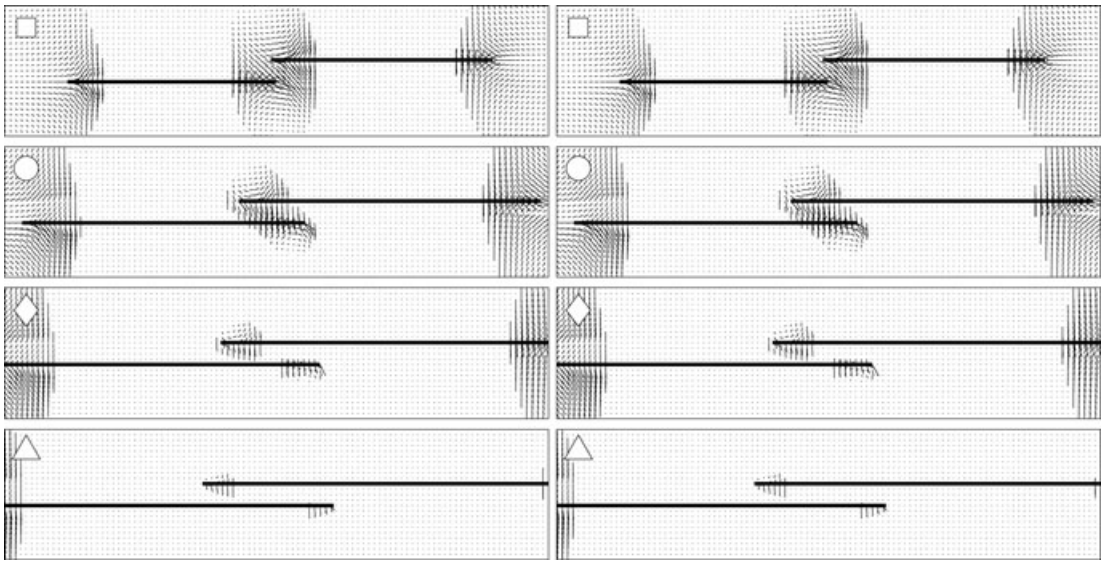

**Figure 15.** Combined representation of the orientation and amplitude of the most sheared plane (plotted only if shear along $x$ is positive) in the relay formed by the non-symmetric simulations 5′ (left-hand panels) and 6′ (right-hand panels). See Table 1 for the parameters. From top to bottom, snapshots correspond to the particular times pointed by squares, circles, diamonds and triangles. These times are defined in Section 6.1 and are reported on Figs 13 and 14 (top panel).

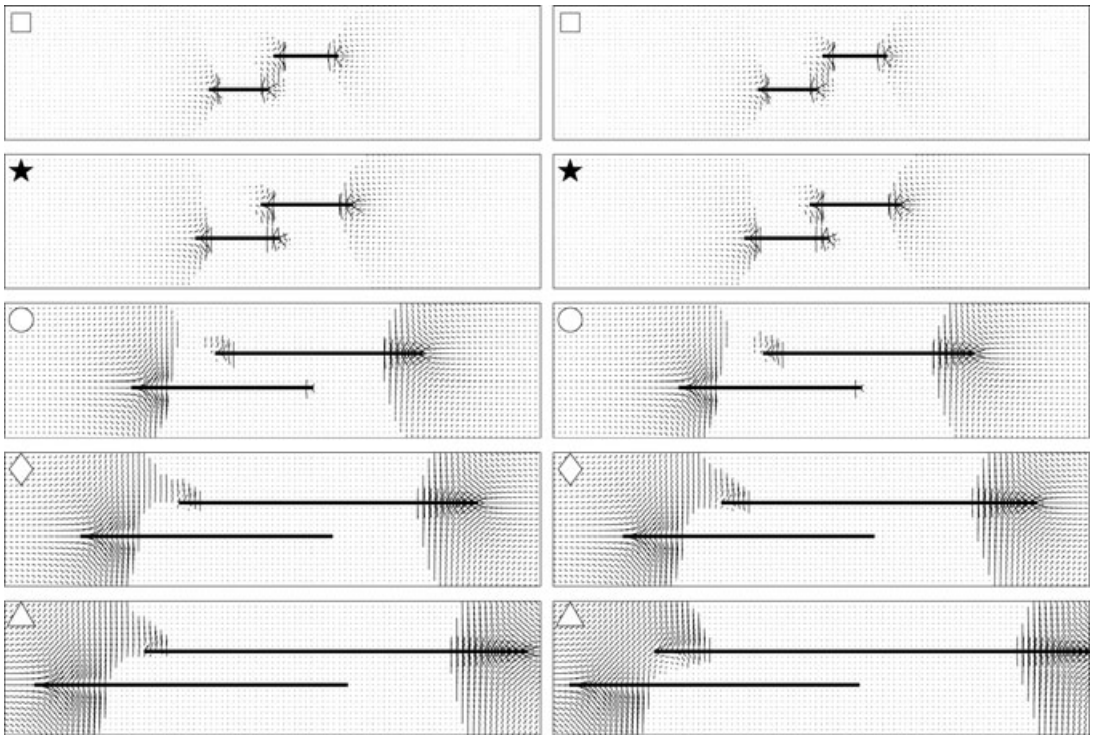

**Figure 16.** Combined representation of the orientation and amplitude of the most sheared plane (plotted only if shear along $x$ is positive) in the relay formed by the non-symmetric simulation 8′ (left-hand panels) and 9′ (right-hand panels). See Table 1 for the parameters. From top to bottom, snapshots correspond to the particular times pointed by squares, stars, circles, diamonds and triangles. These times are defined in Section 6.1 and are reported on Figs 13 and 14 (bottom panel).

also exists between simulations 5′ and 6′ but it involves a very large, unrealistic, relay aspect ratio $r(t)/d$). To finish with, in simulations 7′, 8′ and 9′, the phase of acceleration of inner fault tips vanishes and the deceleration of fault tips, as fault overlap, takes much more time, which indicates little interaction. As expected for this second set of simulations, the experimental criterion for linkage (at the circle) does not correspond to any particular mechanical state in the simulations.

### 6.2 Effect of stress interaction on fault tip velocities and cohesive zones

The kinematics of natural fault systems has been observed by several authors. In Afar, Manighetti *et al.* (2001) studied numerous faults and proposed many scenarios of fault propagation, however their measurements could not directly retrieve the slipping history and especially the variations of their behaviour in time. Recently Taylor *et al.* (2004) performed high resolution imaging of fault systems in the Whakatane Graben (New Zealand) at different times through stratigraphic studies. On the Rangitaiki fault (now fully breached), they could image the changes of slipping rates as fault interact and link. In particular, they could observe the stopping of the propagation of several segments, to the benefit of the development of new linking segments. However it is still very difficult to obtain continuous informations on both slip rates and fault tip propagation. Our quasi-static model predicts that fault tip velocities can be strongly influenced by stress interaction. For example in simulations 4′, 5′ and 6′, we observe that fault tip velocities undergo large variations: from 35 per cent larger values as fault tips approach each other, down to 70 per cent smaller values as fault overlap. These variations strongly depend on the initial fault separation $d/e(0)$. Further investigations are necessary to compare with natural fault systems.

In the model of Cowie & Scholz (1992), the length of the cohesive zone is controlled by the variation of the rock strength around fault tips. In our simulations based on the complete slip-dependent friction (including critical slip-weakening distance and finite stress drop), we find that the length of the cohesive zone can also be strongly dependent on the interaction process. In simulations 1 and 1′, where separation is very small ($d/e(0) = 0.02$), stress interaction is strong and we observe that the length of the cohesive zone at the inner tips is approximately four times smaller than that of the free outer tips. Consequently, the stress field in the relay can be influenced by higher order effects like the possible evolution of the cohesive zone due to stress interaction.

### 6.3 Discussion of mechanical assumptions

Beyond the fact that our model is only bi-dimensional, one of the main objections that can be raised against our model (and against many models used to understand faulting at long timescale) is the use of the linear elastic rheology for the crust. Indeed the use of uniform rates of loading implies that, ahead of the fault tips, the intact crust has either a very low stress or a very large strength to stabilize fault tip propagation. To work with an elastic model, at least one has to keep in mind that damage and multiple relaxations processes will strongly affect the effective stiffness at the tectonic timescale (several orders softer). This can modify both the remote loading process and the interaction between faults, that we have implicitely decoupled. We can make the same remark on the weakening rates that we used to model frictional properties: this weakening must be several orders lower than the seismic weakening used in earthquake modelling, otherwise shear stress would be zero on major faults that have accumulated kilometric slip. When addressing the question of

observed constant fault slip gradients, Bürgmann *et al.* (1994) proposed the introduction of elastic heterogeneities and anelasticity to properly model fault cumulated slips, and Barr & Houseman (1996) proposed a non-linear viscous rheology. Finally, to explain constant fault slip gradients, Cowie & Shipton (1998) proposed a model based on discrete slipping-healing patches to mimic the accumulation of slip by rupture events. All models were satisfactory to model slip gradients and this tends to show that it is still difficult to discriminate the kind of crustal rheology that must be used in faulting models at tectonic timescale.

The second restrictive assumption of our model is the smooth evolution of slip processes and tip propagation, which is due to the use of very regular shapes of strength excess. Although it is possible to introduce heterogeneities, it was out of the scope of this study, and we have assumed that the succession of ruptures (stick-slip) can self-average to produce smooth enough slip profiles. This question has been investigated on real faults by Manighetti *et al.* (2005). However, the dynamic effects of seismic rupture propagation may be crucial for faulting on tectonic timescale. On the seismic timescale, Voisin *et al.* (2002) showed that the use of frictional strengthening is mandatory to stabilize the arrest of dynamic rupture at the tips of a single fault, which makes a significant difference with our purely weakening model. Furthermore, always on seismic timescale, numerous experiments of dynamic rupturing on multiple, en echelon or bend, fault segments have been performed in 2-D and 3-D. On prescribed fault geometries, Harris & Day (1999), Oglesby *et al.* (2003), Aochi & Madariaga (2003) and many other authors studied the behaviour of dynamic rupture, that is, how it jumps, selects fault branches and radiates seismic waves. On tectonic timescale, mechanical energy transfers through earthquakes is small but the shape of fault networks may be strongly determined by the effects of seismic waves. In other words, although faults are not built during the dynamic events only, Kame & Yamashita (1999) showed that dynamic effect on crack growth in intact material strongly determines the crack path and this can have important consequences on the formation of damage and secondary linking faults.

## 7 CONCLUSION

We have built a new simple method to model the 2-D antiplane growth of competing non-coplanar faults in elastic medium, that handles strong stress interaction and slip-dependent friction. The method, based on a Chebyshev representation of fault slip, handles complex slip-dependent frictional behaviours and solves, quasi analytically and without space discretization, the straight propagation of faults. The technique is however partly linearized, since based on the cancelation of stress singularity at fault tips, and it cannot avoid back-slip and back-propagation. We showed that strong interaction impacts the propagation of inner fault tips: it favours acceleration before faults overlap and deceleration afterwards. We found that fault systems subject to constant weakening become unstable and the use of non-linear weakening, through the introduction of a critical weakening distance and a finite stress drop, keeps the system stable much longer, as expected.

To interpret these results, we have re-investigated the spectral analysis that was previously used to interpret the shape of slip profiles in real fault networks by Wolf *et al.* (2006). The spectral analysis takes into account fault interaction. The first mode found by this analysis can be used to interpret the properties of the quasi-static solution. In particular, we found that, for two faults of any lengths $2a$ and $2b$, separation $2d$ and offset $2e$, there is a subset of parameters that links $a$, $b$, $d$ and $e$ such that the first linear mode has a vanishing stress intensity factor at the inner tip of the smallest fault. This phenomenon is related to the strong deceleration and arrest of the fault tip in the quasi-static experiments.

Also, we examined the state of stress at different stages of the quasi-static evolution and compared our results with the experimental data of Soliva & Benedicto (2004). In particular, we investigated the possible influence of the relay aspect ratio (overlap/separation) to interpret several geometrical aspects of the linking process. For small fault separations, we remarked that stress interaction has a very important impact on the deceleration of the inner fault tips, and that the experimental geometrical criterion for linkage (overlap $\gtrsim 2.9 \times$ separation) seems to correspond to the end of this deceleration. Also at that moment, the stress orientation suggests a change of orientation of the faults outwards the relay zone (which is observed on real faults) and a very favouring stress field regarding secondary fracturing (also typically observed in relay ramps).

## ACKNOWLEDGMENTS

Part of the computations has been performed at the parallel computing facility of the Institut de Physique du Globe de Paris. We thank editor Massimo Cocco, reviewers Ruth Harris and David Oglesby and two anonymous reviewers for their very helpful comments.

## REFERENCES

Aochi, H. & Madariaga, R., 2003. The 1999 Izmit, Turkey, earthquake: non planar fault structure, dynamic rupture process and strong ground motion, *Bull. seism. Soc. Am.,* **93,** 1249–1266.

Barr, T.D. & Houseman, G.A., 1996. Deformation fields around a fault embedded in a non-linear ductile medium, *Geophys. J. Int.,* **125,** 473–490.

Barrenblatt, G., I., 1962. The mathematical theory of equilibrium cracks in brittle fracture, *Adv. Appl. Mech.,* **7,** 55–125.

Baud, P. & Reuschlé, T., 1997. A theoretical approach to the propagation of interacting cracks, *Geophys. J. Int.,* **130,** 460–468.

Ben-Zion, Y., Dahmen, K., Lyakovsky, V., Ertas, D. & Agnon, A., 1999. Self driven mode switching of earthquake activity in fault system, *Earth planet. Sci. Lett.,* **172,** 11–21.

Bonafede, M., Dragoni, M. & Boschi, E., 1986. Quasi-static crack models and the frictional stress threshold criterion for slip arrest, *Geophys. J. R. astr. Soc.,* **83,** 615–637.

Bürgmann, R., Pollard, D.D. & Martel, S.J., 1994. Slip distribution on faults: effects of stress gradients, inelastic deformation, heterogeneous host-rock stiffness, and fault interaction, *J. Struct. Geol.,* **16,** 1675–1690.

Chen, Y. & Knopoff, L., 1986. Static shear crack with a zone of slip-weakening, *Geophys. J. R. astr. Soc.,* **87,** 1005–1024.

Cowie, P.A. & Scholz, C.H., 1992. Physical explanation for the displacement-length relationship of faults using a post-yield fracture mechanics model, *J. Struct. Geol.,* **14,** 1133–1148.

Cowie, P.A. & Shipton, Z.K., 1998. Fault tip displacement gradients and process zone dimensions, *J. Struct. Geol.,* **20,** 983–997.

Crider, G.C. & Pollard, D.D., 1998. Fault linkage: three-dimensional mechanical interaction between echelon normal faults, *J. geophys. Res.,* **103,** 24 373–24 391.

Dascalu, C., Ionescu, I.R. & Campillo M., 2000. Fault finiteness and initiation of dynamic shear instability, *Earth planet. Sci. Lett.,* **177,** 163–176.

Gupta, A. & Scholz, C.H., 2000. A model of normal fault interaction based on observations and theory, *J. Struct. Geol.,* **22,** 865–879.

Harris, R.A. & Day, S.M., 1999. Dynamic 3D simulations of earthquakes on en echelon faults, *Geophys. Res. Lett.,* **26,** 2089–2092.

Ionescu, I. & Wolf, S., 2005. Interaction of faults under slip-dependent friction. Non-linear eigenvalue analysis, *Math. Method Appl. Sci.,* **28,** 77–100.

Kame, N. & Yamashita, T., 1999. Simulation of the spontaneous growth of a dynamic crack without constraints on the crack tip path, *Geophys. J. Int.,* **139,** 345–358.
Kame, N., Saito, S. & Oguni, K., 2008. Quasi-static analysis of strike fault growth in layered media, *Geophys. J. Int.,* **173**(1), 309–314, doi:10.1111/j.1365-246X.2008.03728.x.
Lin, J. & Parmentier, M., 1988. Quasistatic propagation of a normal fault: a fracture mechanics model, *J. Struct. Geol.,* **10,** 249–262.
Manighetti, I., King, G.C.P., Gaudemer, Y., Scholz, C.H. & Doubre, C., 2001. Slip accumulation and lateral propagation of active normal faults in Afar, *J. geophys. Res.,* **106,** 13 667–13 696.
Manighetti, I., Campillo, M., Sammis, C.G., Mai, P.M. & King, G., 2005. Evidence for self-similar, triangular slip distributions on earthquakes; implications for earthquake and fault mechanics, *J. geophys. Res.,* **110,** B05302, doi:10.1029/2004JB003174.
Martel, S.J., 1997. Effects of cohesive zones on small faults and implications for secondary fracturing and fault trace geometry, *J. Struct. Geol.,* **19,** 835–847.
Narteau, C., 2007. Formation and evolution of a population of strike-slip faults in a multiscale cellular automaton model, *Geophys. J. Int.,* **168,** 723–744.
Oglesby, D.D., Day, S.M. & O'Connell, D.R.H., 2003. The dynamic and static interaction of two thrust faults: a case study with general implications, *J. geophys. Res.,* **108,** 2489, doi:10.1029/2002JB002228.
Palmer, A.C. & Rice, J.R., 1973. The growth of slip surfaces in the progressive failure of overconsolidated clay, *Proc. R. Soc. Lond.,* **A332**, 527–548.
Peacock, D.C.P., 2002. Propagation, interaction and linkage in normal fault system, *Earth-Sci. Rev.,* **58,** 121–142.
Peacock, D.C.P. & Sanderson, D.J., 1991. Displacements, segment linkage and relay ramps in normal fault zones, *J. Struct. Geol.,* **13,** 721–733.
Segall, P. & Pollard, D.D., 1980. Mechanics of discontinuous faults, *J. geophys. Res.,* **85,** 4337–4350.
Soliva, R. & Benedicto, A., 2004. A linkage criterion for segmented normal faults, *J. Struct. Geol.* **26,** 2251–2257.
Spyropoulos, C., Scholz, C. & Shaw, E., 2002. Transition regimes for growing crack populations, *Phys. Rev. E,* **65,** 056105, doi:10.1103/PhysRevE.65.056105.
Taylor, S.K., Bull, J.M., Lamarche, G. & Barnes, P.M., 2004. Normal fault growth and linkage in the Whakatane Graben, New Zealand, during the last 1.3 Myr, *J. geophys. Res.,* **109,** doi:10.1029/2003JB002412.
Uenishi, K. & Rice, J.R., 2003. Universal nucleation length for slip-weakening rupture instability under nonuniform fault loading *J. geophys. Res.,* **108**(B1), 2042, doi:10.1029/2001JB001681.
Voisin, C., Ionescu, I. & Campillo, M., 2002. Crack growth resistance and dynamic rupture arrest under slip dependent friction, *Phys. Earth planet. Int.,* **131,** 279–274.
Willemse, J.M.E., 1997. Segmented normal faults: correspondence between three-dimensional mechanical models and field data, *J. geophys. Res.,* **102,** 675–692.
Wolf, S., Manighetti, I., Campillo, M. & Ionescu, I.R., 2006. Mechanics of normal fault networks subject to slip-weakening friction, *Geophys. J. Int.,* **165,** 677–691.
Yamashita, T. & Knopoff, L., 1992. Model for intermediate-term precursory clustering of earthquakes, *J. geophys. Res.* **97,** 19 873–19 879.

## APPENDIX A: ELEMENTARY DISPLACEMENTS AND STRESSES FUNCTIONS

In this section, we give simple expressions of displacement, stresses and stress derivatives around a fault segment subject to a particular basis of slip functions.

Let us define $z = x + iy$, with $\{x, y\} \in ]-\infty, \infty[^2$ and $i^2 = -1$. The complex function $\sqrt{z}$ with the branch point $z = 0$ is cut along the branch $z \in ]-\infty, 0[$. Let us define by $U_k$ the $k$th order Chebyshev polynomials of second kind. Then we have, for a single antiplane fault of length 2, located at $\{y = 0, |x| < 1\}$ in an infinite elastic medium of shear modulus 1, and subject to a slip profile $\delta w_k(x) = 2\sin[k \arccos(x)] = 2\sqrt{1-x^2}U_{k-1}(x)$, $k$ integer and strictly positive

$$w_k(x, y) = \mathrm{Im}[F_k(x + iy)] \tag{A1}$$

$$\tau_k(x, y) + i\sigma_k(x, y) = F_k'(x + iy) \tag{A2}$$

$$\frac{\partial}{\partial x}[\tau_k(x, y) + i\sigma_k(x, y)] = F_k''(z) \tag{A3}$$

$$\frac{\partial}{\partial y}[\tau_k(x, y) + i\sigma_k(x, y)] = iF_k''(z) \tag{A4}$$

with

$$F_k(z) = -\left(z + \sqrt{z+1}\sqrt{z-1}\right)^{-k} \tag{A5}$$

$$F_k'(z) = -\frac{kF_k(z)}{\sqrt{z+1}\sqrt{z-1}} \tag{A6}$$

$$F_k''(z) = \frac{k}{\sqrt{z+1}\sqrt{z-1}}\left[\frac{zF_k(z)}{z^2-1} - F_k'(z)\right], \tag{A7}$$

where $w_k(x, y)$, $\sigma_k(x, y)$ and $\tau_k(x, y)$ are displacements and stresses in the whole body.

The asymptotic fields around the fault tips are deduced from the following series, $\forall\epsilon > 0$, $\forall\phi \in [-\pi, \pi]$:

$$F_k(\pm 1 \pm \epsilon e^{i\phi}) = (\pm 1)^k\left(-1 + k\sqrt{2\epsilon}e^{i\frac{\phi}{2}}\right) + o(\epsilon) \tag{A8}$$

$$F_k'(\pm 1 \pm \epsilon e^{i\phi}) = (\pm 1)^{k-1}k\left(\frac{e^{-i\frac{\phi}{2}}}{\sqrt{2\epsilon}} - k\right) + o(\epsilon) \tag{A9}$$

which gives finally $\forall\epsilon > 0$, $\forall\phi \in [-\pi, \pi]$

$$w_k[\pm 1 \pm \epsilon\cos(\phi), \pm\epsilon\sin(\phi)] = (\pm 1)^k k\sqrt{2\epsilon}\sin\left(\frac{\phi}{2}\right) + o(\epsilon) \tag{A10}$$

$$\sigma_k[\pm 1 \pm \epsilon\cos(\phi), \pm\epsilon\sin(\phi)] = (\pm 1)^{k-1}\frac{-k\sin\left(\frac{\phi}{2}\right)}{\sqrt{2\epsilon}} + o(\epsilon) \tag{A11}$$

$$\tau_k[\pm 1 \pm \epsilon\cos(\phi), \pm\epsilon\sin(\phi)] = (\pm 1)^{k-1}k\left[\frac{\cos\left(\frac{\phi}{2}\right)}{\sqrt{2\epsilon}} - k\right] + o(\epsilon). \tag{A12}$$

Stress intensity corresponds to the amplitude (multiplied by $\sqrt{2\pi}$) of the first term of the upper asymptotic development of stresses (i.e. the inverse square root term), regardless of the angular dependence. It follows that the associated stress intensity factors are $K_k^+ = k\sqrt{\pi}$ for the right tip and $K_k^- = (-1)^{k-1}k\sqrt{\pi}$ for the left one.

## APPENDIX B: SERIES EXPANSION FOR TWO FAULTS

Let us consider two faults $\Gamma_a$ and $\Gamma_b$ parallel to $x$ and non-coplanar. Fault $\Gamma_a$ has length $2a$ and is located at $\{y = -d, |x + e| < a\}$. Fault $\Gamma_b$ has length $2b$ and is located at $\{y = d, |x - e| < b\}$ . $\mu$

denotes the shear modulus. On both faults, we introduce the change of abscissa $\{x = -e + a\cos(\theta), \theta \in [0, \pi]\}$ on $\Gamma_a$ and $\{x = e + b\cos(\theta), \theta \in [0, \pi]\}$ on $\Gamma_b$. Following this, we write for any function $f_a$ on $\Gamma_a$ and $f_b$ on $\Gamma_b$: $f_a(x) = \tilde{f}_a(\theta)$ and $f_b(x) = \tilde{f}_b(\theta)$. Finally, the unknown slip functions are defined by

$$\delta\tilde{w}_a(\theta) = \sum_{k=1}^{N} W_{ak}\delta w_k(\cos\theta) = 2\sum_{k=1}^{N} W_{ak}\sin(k\theta) \tag{B1}$$

$$\delta\tilde{w}_b(\theta) = \sum_{k=1}^{N} W_{bk}\delta w_k(\cos\theta) = 2\sum_{k=1}^{N} W_{bk}\sin(k\theta), \tag{B2}$$

where $W_{ak}$ and $W_{bk}$ are $2N$ real coefficients. This definition assumes an expansion of both fault slips on the basis of functions $\delta w_k$ defined previously. Here the expansion is finite, for numerical purposes, but the true solution is obtained when $N \to \infty$.

Displacement and stresses are deduced by summation. Remarking that $\tau_k(\cos\theta, 0) = -k\sin(k\theta)/\sin(\theta)$, the shear stress field acting on each fault is

$$\tilde{\tau}_a(\theta) = -\frac{\mu}{a}\sum_{k=1}^{N} W_{ak}\frac{k\sin(k\theta)}{\sin(\theta)} + \frac{\mu}{b}\sum_{k=1}^{N} W_{bk}\tau_k\left(\frac{-2e + a\cos\theta}{b}, \frac{-2d}{b}\right) \tag{B3}$$

$$\tilde{\tau}_b(\theta) = -\frac{\mu}{b}\sum_{k=1}^{N} W_{bk}\frac{k\sin(k\theta)}{\sin(\theta)} + \frac{\mu}{a}\sum_{k=1}^{N} W_{ak}\tau_k\left(\frac{+2e + b\cos\theta}{a}, \frac{+2d}{a}\right). \tag{B4}$$

For both faults, the shear stress caused by the other slipping fault is not singular and only their own slip can be singular at the tips. The stress intensity factors of the four fault tips are

$$K_a^{\pm} = \mu\sqrt{\frac{\pi}{a}}\sum_{k=1}^{N} W_{ak}(\pm 1)^{k-1}k \tag{B5}$$

$$K_b^{\pm} = \mu\sqrt{\frac{\pi}{b}}\sum_{k=1}^{N} W_{bk}(\pm 1)^{k-1}k. \tag{B6}$$

$K_a^+ = 0$, $K_a^- = 0$, $K_b^+ = 0$ and $K_b^- = 0$, respectively, are the conditions to have a finite shear stress at right/left $\Gamma_a$ tips and right/left $\Gamma_b$ tips, respectively.

## APPENDIX C: QUASI-STATIC PROBLEM FOR TWO WEAKENING FAULTS

Following Section 4, we have to solve (13), (14) and (15), that we rewrite $\forall\,\theta \in [0, \pi]$:

$$\tilde{\tau}_a(\theta) = \tau_a^e[c - e + a\cos(\theta)] - \alpha_a\frac{\delta\tilde{w}_a(\theta)}{2} + \tau_a^r[\delta\tilde{w}_a(\theta)] \tag{C1}$$

$$K_a^+ = 0 \tag{C2}$$

$$K_a^- = 0 \tag{C3}$$

$$\tilde{\tau}_b(\theta) = \tau_b^e[c + e + b\cos(\theta)] - \alpha_b\frac{\delta\tilde{w}_b(\theta)}{2} + \tau_b^r[\delta\tilde{w}_b(\theta)] \tag{C4}$$

$$K_b^+ = 0 \tag{C5}$$

$$K_b^- = 0, \tag{C6}$$

where the tilding of functions denotes the change of variable $x$ to $\theta$, such that $x = c - e + a\cos(\theta)$ on $\Gamma_a$ and $x = c + e + b\cos(\theta)$ on $\Gamma_b$.

Using the series expansion as defined in Appendix B (see eqs B1, B2, B3 and B4), we can reformulate (C1) and (C4) as series. After, we multiply these series by $\frac{2}{\pi\mu}\sin^q(\theta)\sin(m\theta)$ and integrate for $\theta$isin; $[0, \pi]$. We have chosen $q = 0$ as in (Uenishi & Rice 2003). By using (B5) and (B6), we also reformulate (C2), (C3), (C5) and (C6) and we obtain $\forall\, m \in 1, \ldots, N$

$$\mathcal{S}_{am} = \sum_{k=1}^{N}\left(\frac{M_m^k}{a}W_{ak} - \frac{R_m^k}{b}W_{bk}\right) + T_{am} - \frac{\alpha_a}{\mu}W_{am} + X_{am} = 0 \tag{C7}$$

$$K_a^+ = \sum_{k=1}^{N} W_{ak}k = 0 \tag{C8}$$

$$K_a^- = \sum_{k=1}^{N} W_{ak}(-1)^{k-1}k = 0 \tag{C9}$$

$$\mathcal{S}_{bm} = \sum_{k=1}^{N}\left(\frac{M_m^k}{b}W_{bk} - \frac{L_m^k}{a}W_{ak}\right) + T_{bm} - \frac{\alpha_b}{\mu}W_{bm} + X_{bm} = 0 \tag{C10}$$

$$K_b^+ = \sum_{k=1}^{N} W_{bk}k = 0 \tag{C11}$$

$$K_b^- = \sum_{k=1}^{N} W_{bk}(-1)^{k-1}k = 0 \tag{C12}$$

with

$$T_{am} = \frac{2}{\pi\mu}\int_0^{\pi}\tau_a^e[c - e + a\cos(\theta)]\sin(m\theta)\mathrm{d}\theta$$
$$X_{am} = \frac{2}{\pi\mu}\int_0^{\pi}\tau_a^r\left[2\sum_{k=1}^{N}W_{ak}\sin(k\theta)\right]\sin(m\theta)\mathrm{d}\theta$$
$$T_{bm} = \frac{2}{\pi\mu}\int_0^{\pi}\tau_b^e[c + e + b\cos(\theta)]\sin(m\theta)\mathrm{d}\theta$$
$$X_{bm} = \frac{2}{\pi\mu}\int_0^{\pi}\tau_b^r\left[2\sum_{k=1}^{N}W_{bk}\sin(k\theta)\right]\sin(m\theta)\mathrm{d}\theta$$

and with

$$M_m^k = \frac{2k}{\pi}\int_0^{\pi}\frac{\sin(k\theta)\sin(m\theta)}{\sin\theta}\mathrm{d}\theta = \frac{k}{\pi}[1 + (-1)^{k+m}]\sum_{p=1+|k-m|}^{k+m-1}\frac{1 - (-1)^p}{p} \tag{C13}$$

$$R_m^k = \frac{2}{\pi}\int_0^{\pi}\tau_k\left(\frac{-2e + a\cos\theta}{b}, \frac{-2d}{b}\right)\sin(m\theta)\mathrm{d}\theta \tag{C14}$$

$$L_m^k = \frac{2}{\pi}\int_0^{\pi}\tau_k\left(\frac{+2e + b\cos\theta}{a}, \frac{+2d}{a}\right)\sin(m\theta)\mathrm{d}\theta. \tag{C15}$$

Eqs (C7)–(C12) form a $2N + 4$ non linear system of equations. Terms $M_m^k$ which represent the self-influence of the faults (the singular part of the problem) are determined analytically by (C13). Terms $R_m^k$ and $L_m^k$ represent the cross-influence of the faults and they remain as integrals (see C14 and C15) since they contain to much parameters to hope a simple analytical expression. However, their integrand is regular at all order, therefore $R_m^k$ and $L_m^k$ scalars can be computed by a high-order numerical integration method.

If the functions $\tau_a^r$ and $\tau_b^r$ are sufficiently smooth functions of the displacement, each equation of this system depends smoothly of the $2N + 4$ unknowns, that is, the $NW_ak$ numbers, the $NW_bk$ numbers, $a$, $b$, $c$ and $e$. This property combined with the assumption that the system remains non singular allows us to use the classical iterative Newton method to solve it. This needs to compute the Jacobian of the system. Fortunately, after a few algebra, it can be computed accurately with the following formulae:

$$\frac{\partial \mathcal{S}_{am}}{\partial W_{aj}} = \frac{M_m^j}{a} - \frac{\alpha_a}{\mu}\delta_{mj} + 2X_{a,m}^j$$

$$\frac{\partial \mathcal{S}_{am}}{\partial W_{bj}} = -\frac{R_m^j}{b}$$

$$\frac{\partial \mathcal{S}_{am}}{\partial a} = -\sum_{k=1}^{N}\left(\frac{M_m^k}{a^2}W_{ak} + \frac{R_{1,m}^k}{b^2}W_{bk}\right) + T_{a,1,m}$$

$$\frac{\partial \mathcal{S}_{am}}{\partial b} = \frac{1}{b^2}\sum_{k=1}^{N}\left(R_m^k - \frac{2dR_{2,m}^k}{b} - \frac{2eR_{0,m}^k}{b} + \frac{aR_{1,m}^k}{b}\right)W_{bk}$$

$$\frac{\partial \mathcal{S}_{am}}{\partial c} = T_{a,0,m}$$

$$\frac{\partial \mathcal{S}_{am}}{\partial e} = \sum_{k=1}^{N}\frac{2R_{0,m}^k}{b^2}W_{bk} - T_{a,0,m}$$

$$\frac{\partial K_a^+}{\partial W_{aj}} = j,\ \frac{\partial K_a^-}{\partial W_{aj}} = (-1)^{j-1}j$$

$$\frac{\partial K_a^\pm}{\partial W_{bj}} = \frac{\partial K_a^\pm}{\partial a} = \frac{\partial K_a^\pm}{\partial b} = \frac{\partial K_a^\pm}{\partial c} = \frac{\partial K_a^\pm}{\partial e} = 0$$

$$\frac{\partial \mathcal{S}_{bm}}{\partial W_{aj}} = -\frac{L_m^j}{a}$$

$$\frac{\partial \mathcal{S}_{bm}}{\partial W_{bj}} = \frac{M_m^j}{b} - \frac{\alpha_b}{\mu}\delta_{mj} + 2X_{b,m}^j$$

$$\frac{\partial \mathcal{S}_{bm}}{\partial a} = \frac{1}{a^2}\sum_{k=1}^{N}\left(L_m^k + \frac{2dL_{2,m}^k}{a} + \frac{2eL_{0,m}^k}{a} + \frac{bL_{1,m}^k}{a}\right)W_{ak}$$

$$\frac{\partial \mathcal{S}_{bm}}{\partial b} = -\sum_{k=1}^{N}\left(\frac{M_m^k}{b^2}W_{bk} + \frac{L_{1,m}^k}{a^2}W_{ak}\right) + T_{b,1,m}$$

$$\frac{\partial \mathcal{S}_{bm}}{\partial c} = T_{b,0,m}$$

$$\frac{\partial \mathcal{S}_{bm}}{\partial e} = -\sum_{k=1}^{N}\frac{2L_{0,m}^k}{a^2}W_{ak} + T_{b,0,m}$$

$$\frac{\partial K_b^+}{\partial W_{bj}} = j,\ \frac{\partial K_b^-}{\partial W_{bj}} = (-1)^{j-1}j$$

$$\frac{\partial K_b^\pm}{\partial W_{aj}} = \frac{\partial K_b^\pm}{\partial a} = \frac{\partial K_b^\pm}{\partial b} = \frac{\partial K_b^\pm}{\partial c} = \frac{\partial K_b^\pm}{\partial e} = 0$$

with

$$T_{a,0,m} = \frac{2}{\pi\mu}\int_0^\pi \tau_a^{e\prime}(c - e + a\cos(\theta))\sin(m\theta)\mathrm{d}\theta$$

$$T_{a,1,m} = \frac{2}{\pi\mu}\int_0^\pi \cos(\theta)\tau_a^{e\prime}(c - e + a\cos(\theta))\sin(m\theta)\mathrm{d}\theta$$

$$T_{b,0,m} = \frac{2}{\pi\mu}\int_0^\pi \tau_b^{e\prime}(c + e + b\cos(\theta))\sin(m\theta)\mathrm{d}\theta$$

$$T_{b,1,m} = \frac{2}{\pi\mu}\int_0^\pi \cos(\theta)\tau_b^{e\prime}(c + e + b\cos(\theta))\sin(m\theta)\mathrm{d}\theta$$

$$X_{a,m}^k = \frac{2}{\pi\mu}\int_0^\pi \tau_a^{r\prime}\left(2\sum_{l=1}^{N}W_{al}\sin(l\theta)\right)\sin(k\theta)\sin(m\theta)\mathrm{d}\theta$$

$$X_{b,m}^k = \frac{2}{\pi\mu}\int_0^\pi \tau_b^{r\prime}\left(2\sum_{l=1}^{N}W_{bl}\sin(l\theta)\right)\sin(k\theta)\sin(m\theta)\mathrm{d}\theta$$

$$R_{0,m}^k = \frac{2}{\pi}\int_0^\pi \frac{\partial\tau_k}{\partial x}\left(\frac{-2e + a\cos\theta}{b}, \frac{-2d}{b}\right)\sin(m\theta)\mathrm{d}\theta$$

$$R_{1,m}^k = \frac{2}{\pi}\int_0^\pi \cos(\theta)\frac{\partial\tau_k}{\partial x}\left(\frac{-2e + a\cos\theta}{b}, \frac{-2d}{b}\right)\sin(m\theta)\mathrm{d}\theta$$

$$R_{2,m}^k = \frac{2}{\pi}\int_0^\pi \frac{\partial\tau_k}{\partial y}\left(\frac{-2e + a\cos\theta}{b}, \frac{-2d}{b}\right)\sin(m\theta)\mathrm{d}\theta$$

$$L_{0,m}^k = \frac{2}{\pi}\int_0^\pi \frac{\partial\tau_k}{\partial x}\left(\frac{2e + b\cos\theta}{a}, \frac{2d}{a}\right)\sin(m\theta)\mathrm{d}\theta$$

$$L_{1,m}^k = \frac{2}{\pi}\int_0^\pi \cos(\theta)\frac{\partial\tau_k}{\partial x}\left(\frac{2e + b\cos\theta}{a}, \frac{2d}{a}\right)\sin(m\theta)\mathrm{d}\theta$$

$$L_{2,m}^k = \frac{2}{\pi}\int_0^\pi \frac{\partial\tau_k}{\partial y}\left(\frac{2e + b\cos\theta}{a}, \frac{2d}{a}\right)\sin(m\theta)\mathrm{d}\theta.$$

It is also noticeable that, when the friction laws are linear (i.e $\tau_a^r$ and $\tau_b^r$ are set to zero), then the computation is much faster because not only the costly terms $X_{am}$, $X_{bm}$, $X_{a,m}^k$ and $X_{b,m}^k$ vanish but also the system becomes linearly dependent of the $2N$ scalars $W_{ak}$ and $W_{bk}$, which accelerates the convergence.

## APPENDIX D: LINEAR SPECTRAL PROBLEM FOR TWO WEAKENING FAULTS

Following Section 5, we have to solve (26) and (27, that we rewrite $\forall\theta \in [0, \pi]$:

$$\tilde{\tau}_a(\theta) = -\alpha\delta\tilde{w}_a(\theta)/2 \qquad \text{(D1)}$$

$$\tilde{\tau}_b(\theta) = -\alpha\delta\tilde{w}_b(\theta)/2, \tag{D2}$$

where the tilding of functions denotes the change of variable $x$ to $\theta$, such that $x = c - e + a\cos(\theta)$ on $\Gamma_a$ and $x = c + e + b\cos(\theta)$ on $\Gamma_b$.

Using the series expansion as defined in Appendix B (see eqs B1, B2, B3 and B4), we can reformulate (D1) and (D2) as series. After, we multiply these series by $\frac{2}{\pi\mu}\sqrt{ab}\sin^q(\theta)\sin(m\theta)$ and integrate for $\theta \in [0, \pi]$. We have chosen $q = 0$ as in (Uenishi & Rice 2003). We obtain $\forall\, m \in 1, \ldots, N$:

$$\sum_{k=1}^{N} \sqrt{\frac{b}{a}} M_m^k W_{ak} - \sqrt{\frac{a}{b}} R_m^k W_{bk} = \beta W_{am} \tag{D3}$$

$$\sum_{k=1}^{N} \sqrt{\frac{a}{b}} M_m^k W_{bk} - \sqrt{\frac{b}{a}} L_m^k W_{ak} = \beta W_{bm}, \tag{D4}$$

where $\beta = \frac{\alpha}{\mu}\sqrt{ab}$ is dimensionless and where $M_m^k$, $R_m^k$, $L_m^k$ are defined in Appendix C by eqs (C13), (C14) and (C15).

Consider the vector $W = [W_{a1}, \ldots, W_{aN}, W_{b1}, \ldots, W_{bN}]$. (D3) and (D4) can be assembled into a four-blocks matrix $A$ to form the $2N \times 2N$ eigenvalue problem $AW = \beta W$ with

$$A = \begin{bmatrix} \left[\sqrt{\frac{b}{a}} M_m^k\right]_{\substack{m\le N \\ k\le N}} & \left[-\sqrt{\frac{a}{b}} R_m^k\right]_{\substack{m\le N \\ k\le N}} \\ \left[-\sqrt{\frac{b}{a}} L_m^k\right]_{\substack{m\le N \\ k\le N}} & \left[\sqrt{\frac{a}{b}} M_m^k\right]_{\substack{m\le N \\ k\le N}} \end{bmatrix}. \tag{D5}$$

It must be noticed that Matrix $A$ is not symmetric. Both diagonal blocks represent the self-influence of the faults (the singular part of the problem). The non-diagonal blocks represent the cross-influence of the faults.